

Observing the Galaxy's massive black hole with gravitational wave bursts

C. P. L. Berry¹* and J. R. Gair¹

¹Institute of Astronomy, University of Cambridge, Madingley Road, Cambridge, CB3 0HA

15 January 2013

ABSTRACT

An extreme-mass-ratio burst (EMRB) is a gravitational wave signal emitted when a compact object passes through periapsis on a highly eccentric orbit about a much more massive body, in our case a stellar mass object about a $10^6 M_\odot$ black hole. EMRBs are a relatively unexplored means of probing the spacetime of massive black holes (MBHs). We conduct an investigation of the properties of EMRBs and how they could allow us to constrain the parameters, such as spin, of the Galaxy's MBH. We find that if an EMRB event occurs in the Galaxy, it should be detectable for periapse distances $r_p < 65r_g$ for a $\mu = 10M_\odot$ orbiting object, where $r_g = GM_\bullet/c^2$ is the gravitational radius. The signal-to-noise ratio scales as $\log(\rho) \simeq -2.7\log(r_p/r_g) + \log(\mu/M_\odot) + 4.9$. For periapses $r_p \lesssim 10r_g$, EMRBs can be informative, and provide good constraints on both the MBH's mass and spin. Closer orbits provide better constraints, with the best giving accuracies of better than one part in 10^4 for both the mass and spin parameter.

Key words: black hole physics – Galaxy: centre – gravitational waves – methods: data analysis.

1 BACKGROUND AND INTRODUCTION

Many, if not all, galactic nuclei have harboured a massive black hole (MBH) during their evolution (Lynden-Bell & Rees 1971; Rees 1984). Observations show there exist well-defined correlations between the MBHs' masses and the properties of their host galaxies, such as bulge luminosity, mass, velocity dispersion and light concentration (e.g. Kormendy & Richstone 1995; Magorrian et al. 1998; Graham et al. 2001; Tremaine et al. 2002; Graham et al. 2011). These suggest coeval evolution of the MBH and galaxy (Peng 2007; Jahnke & Macciò 2011), possibly with feedback mechanisms coupling the two (Haiman & Quataert 2004; Volonteri & Natarajan 2009). The MBH and the surrounding spheroidal component share a common history, such that the growth of one can inform us about the growth of the other.

The best opportunity to study MBHs comes from the compact object in our own Galactic Centre (GC), which is coincident with Sagittarius A* (Sgr A*). Through careful monitoring of stars orbiting the GC, this has been identified as an MBH of mass $M_\bullet = 4.31 \times 10^6 M_\odot$ at a distance of only $R_0 = 8.33$ kpc (Gillessen et al. 2009).

According to the no-hair theorem, the MBH should be described completely by just its mass M_\bullet and spin a , since we expect the charge of an astrophysical black hole (BH) to

be negligible (Chandrasekhar 1998). The spin parameter a is related to the BH's angular momentum J by

$$J = M_\bullet ac; \quad (1)$$

it is often convenient to use the dimensionless spin

$$a_* = \frac{cJ}{GM_\bullet^2}. \quad (2)$$

As we have a good estimate of the mass, to gain a complete description of the MBH we have only to measure its spin; this shall give us insight into its history and role in the evolution of the Galaxy.

The spin of an MBH is determined by several competing processes. An MBH accumulates mass and angular momentum through accretion (Volonteri 2010). Accretion from a gaseous disc shall spin up the MBH, potentially leading to high spin values (Volonteri et al. 2005); a series of randomly orientated accretion events leads to a low spin value: we expect an average value $|a_*| \sim 0.1\text{--}0.3$ (King & Pringle 2006). The MBH also grows through mergers (Yu & Tremaine 2002; Malbon et al. 2007). Minor mergers with smaller BHs can decrease the spin (Hughes & Blandford 2003), while a series of major mergers, between similar mass MBHs, would lead to a likely spin of $|a_*| \sim 0.69$ (Berti et al. 2007; González et al. 2007). Measuring the spin of MBHs shall help us understand the relative importance of these processes, and perhaps gain a glimpse into their host galaxies' pasts.

* E-mail: cplb2@cam.ac.uk

Elliptical and spiral galaxies are believed to host MBHs of differing spins because of their different evolutions: we expect MBHs in elliptical galaxies to have on average higher spins than MBHs in spiral galaxies, where random, small accretion episodes have played a more important role (Volonteri, Sikora, & Lasota 2007; Sikora, Stawarz, & Lasota 2007).

It has been suggested that the spin of the Galaxy's MBH could be inferred from careful observation of the orbits of stars within a few milliparsecs of the GC (Merritt et al. 2010), although this is complicated because of perturbations due to other stars, or from observations of quasi-periodic oscillations in the luminosity of flares believed to originate from material orbiting close to the innermost stable orbits (Genzel et al. 2003; Hamaus et al. 2009), though there are difficulties in interpreting these results (Psaltis 2008).

This latter method, combined with a disc-seismology model, has produced a value of the dimensionless spin of $a_* = 0.44 \pm 0.08$. To obtain this result Kato et al. (2010) have combined their observations of Sgr A* with observations of galactic X-ray sources containing solar mass BHs, to find a best-fit unique spin parameter for all BHs. It is not clear that all BHs should share the same spin parameter; especially as the BHs considered here differ in mass by six orders of magnitude. Even if BH spin is determined by a universal process, we expect some distribution of spin parameters (King, Pringle, & Hofmann 2008; Berti & Volonteri 2008). Thus we cannot precisely determine the spin of the GC's MBH from an average.

The spins of MBHs in active galactic nuclei have been inferred using X-ray observations of Fe K emission lines (Miller 2007; McClintock et al. 2011). This has been done for a handful of other galaxies' MBHs (Brenneman & Reynolds 2006; Miniutti et al. 2009; Schmoll et al. 2009; de la Calle Pérez et al. 2010; Zoghbi et al. 2010; Nardini et al. 2011; Patrick et al. 2011). Estimates for the spin cover a range up to the maximal value for an extremal Kerr BH. Typical results are in the intermediate range of $a_* \sim 0.7$ with an uncertainty of about 10% on each measurement.

While we can use the spin of other BHs as a prior, to inform us of what we should expect for the Galaxy's MBH, it is desirable to have an independent observation, a direct measurement.

An exciting means of inferring information about the MBH is through gravitational waves (GWs) emitted when compact objects (COs), such as stellar mass BHs, neutron stars (NSs), white dwarfs (WDs) or low mass main sequence (MS) stars, pass close by (Sathyaprakash & Schutz 2009). A space-borne detector, such as the *Laser Interferometer Space Antenna* (*LISA*) or the *evolved Laser Interferometer Space Antenna* (*eLISA*), is designed to be able to detect GWs in the frequency range of interest for these encounters (Bender et al. 1998; Danzmann & Rüdiger 2003; Jennrich et al. 2011; Amaro-Seoane et al. 2012a,b).¹ The identification of waves requires a set of accurate waveform templates covering parameter space. Much work has al-

ready been done on the waveforms generated when companion objects inspiral towards an MBH (Glampedakis 2005; Barack 2009); as they orbit, GWs carry away energy and angular momentum, causing the orbit to shrink until eventually the CO plunges into the MBH. The initial orbits may be highly elliptical and a burst of radiation is emitted during each close encounter. These are extreme mass-ratio bursts (EMRBs; Rubbo, Holley-Bockelmann, & Finn 2006). Assuming the companion is not scattered, and does not plunge straight into the MBH, its orbit evolves, becoming more circular, and it begins to continuously emit significant gravitational radiation in the *LISA/eLISA* frequency range. The resulting signals are extreme mass-ratio inspirals (EMRIs; Amaro-Seoane et al. 2007; Amaro-Seoane 2012).

Studies of these systems have usually focused upon the phase when the orbit is close to plunge and completes a large number of cycles in the detector's frequency band, allowing a high signal-to-noise ratio (SNR) to be accumulated. Here, we investigate high eccentricity orbits. These are the initial bursting orbits from which an EMRI may evolve, and are the consequence of scattering from two body encounters. The event rate for the detection of such EMRBs with *LISA* has been estimated to be as high as 15 yr^{-1} (Rubbo et al. 2006), although this has been subsequently revised downwards to the order of 1 yr^{-1} (Hopman, Freitag, & Larson 2007). Even if only a single burst is detected during a mission, this is still an exciting possibility since the information carried by the GW gives an unparalleled probe of the spacetime of the GC. Exactly what can be inferred depends upon the orbit, which we investigate here.

We make the simplifying assumption that all these orbits are marginally bound, or parabolic, since highly eccentric orbits appear almost indistinguishable from an appropriate parabolic orbit. Here "parabolic" and "eccentricity" refer to the energy of the geodesic and not to the geometric shape of the orbit.² Following such a trajectory an object may make just one pass of the MBH or, if the periapsis distance is small enough, it may complete a number of rotations. Such an orbit is referred to as zoom-whirl (Glampedakis & Kennefick 2002).

In order to compute the gravitational waveform produced in such a case, we integrate the geodesic equations for a parabolic orbit in Kerr spacetime. We assume the orbiting body is a test particle, such that it does not influence the underlying spacetime, and that the orbital parameters evolve negligibly during the orbit such that they may be held constant. We use this to construct an approximate numerical kludge (NK) waveform (Babak et al. 2007).

This paper is organised as follows. We begin in Sec. 2 with the construction of the geodesic orbits; these trajectories are used for the NK waveforms as explained in Sec. 3. In Sec. 4 we establish what the *LISA* detectors would measure and how the signal would be analysed. This includes a brief mention of window functions which is expanded in Appendix A. Here we present a novel window function, the Planck-Bessel window, of use for signals with a large dynamic range. In Sec. 5 we look at our NK waveforms. We give fiducial power-law fits for SNR as a function of peri-

¹ The revised *eLISA* concept shares the same descoped design as the *New Gravitational-wave Observatory* (*NGO*) submitted to the European Space Agency for their L1 mission selection.

² Marginally bound Keplerian orbits in flat spacetime are parabolic in both senses.

apse radius, useful for back-of-the-envelope estimates. We confirm the accuracy of the kludge waveforms in Sec. 6 by comparing the energy flux to fluxes calculated using other approaches. The typical error introduced by the NK approximation may be a few percent, but this worsens as the periapsis approaches the last non-plunging orbit. We explain how to extract the information from the bursts in Sec. 7. Results estimating the measurement precision are presented in Sec. 8. We briefly mention the possibility of detecting bursts from extra-galactic sources in Sec. 9, before concluding in Sec. 10 with a summary of our results. EMRBs may be informative if the event rate is high enough for them to be a viable source.

There are currently no funded space-borne detector missions. The *eLISA* mission concept remains an active field of study. It is hoped to submit this to the European Space Agency as a potential cornerstone mission. We use the classic *LISA* design. This is done from historical affection in lieu of a definite alternative. Should funding for a space-borne detector be secured in the future it is hoped that it shall have comparable sensitivity to *LISA*, and that studies using the *LISA* design shall be a sensible benchmark for comparison. We find that to obtain good results the periapse radius must be $r_p \lesssim 10r_g$, where $r_g = GM_\bullet/c^2$ is a gravitational radius; at this point the SNR is already high: for parameter estimation the orbit is more important than the signal strength, and so the exact detector performance should be of secondary importance.

We adopt a metric with signature $(+, -, -, -)$. Greek indices are used to represent spacetime indices $\mu = \{0, 1, 2, 3\}$ and lowercase Latin indices from the middle of the alphabet are used for spatial indices $i = \{1, 2, 3\}$. Uppercase Latin indices from the beginning of the alphabet are used for the output of the two *LISA* detector-arms $A = \{\text{I}, \text{II}\}$, and lowercase Latin indices from the beginning of the alphabet are used for parameter space. Summation over repeated indices is assumed unless explicitly noted otherwise. Geometric units with $G = c = 1$ are used where noted, but in general factors of G and c are retained.

2 PARABOLIC ORBITS IN KERR SPACETIME

Astrophysical BHs are described by the Kerr metric (Kerr 1963). This is conveniently written in terms of Boyer-Lindquist coordinates $\{t, r, \theta, \phi\}$ (Boyer & Lindquist 1967; Hobson, Efstathiou, & Lasenby 2006, section 13.7). For this section we shall work in natural units with $G = c = 1$.

Geodesics are parametrized by three conserved quantities (aside from the particle's mass μ): energy (per unit mass) E , specific angular momentum about the symmetry axis (the z -axis) L_z , and Carter constant Q (Carter 1968; Chandrasekhar 1998, section 62). For a parabolic orbit $E = 1$; the particle is at rest at infinity. This simplifies the geodesic equations. It also allows us to give a simple interpretation for the Carter constant: this is defined as

$$Q = L_\theta^2 + \cos^2 \theta \left[a^2 (1 - E^2) + \frac{L_z^2}{\sin^2 \theta} \right], \quad (3)$$

where L_θ is the (non-conserved) specific angular momentum

in the θ -direction. For $E = 1$

$$Q = L_\theta^2 + \cot^2 \theta L_z^2 = L_\infty^2 - L_z^2; \quad (4)$$

here L_∞ is the total specific angular momentum at infinity, where the metric is asymptotically flat (de Felice 1980).³ This is as in Schwarzschild spacetime.

2.1 Integration variables and turning points

In integrating the geodesic equations, difficulties can arise because of the presence of turning points, when the sign of the r or θ geodesic equation changes. The radial turning points are at the periapsis r_p and at infinity. We may locate the periapsis by finding the roots of

$$V_r = 2M_\bullet r^3 - (L_z^2 + Q)r^2 + 2M_\bullet [(L_z - a)^2 + Q]r - a^2 Q = 0. \quad (5)$$

This has three roots, which we denote $\{r_1, r_2, r_p\}$; the periapsis r_p is the largest real root. We do not find the apoapsis as a (fourth) root as we have removed it by taking $E = 1$ before solving.⁴

We avoid the difficulties associated with the turning point by introducing angular variables that always increase with proper time (Drasco & Hughes 2004): inspired by Keplerian orbits

$$r = \frac{p}{1 + e \cos \psi}, \quad (6)$$

where $e = 1$ is the eccentricity and $p = 2r_p$ is the semilatus rectum. As ψ covers its range from $-\pi$ to π , r traces out a complete orbit. The geodesic equation for ψ is

$$(r^2 + a^2 \cos^2 \theta) \frac{d\psi}{d\tau} = \left\{ M_\bullet \left[2r_p - (r_1 + r_2)(1 + \cos \psi) + \frac{r_1 r_2}{2r_p} (1 + \cos \psi)^2 \right] \right\}^{1/2}, \quad (7)$$

for proper time τ . Parametrizing an orbit by its periapsis and eccentricity has the additional benefit of allowing easier comparison with its flat-space equivalent (Gair, Kennefick, & Larson 2005).

The θ motion is usually bounded, with $\theta_0 \leq \theta \leq \pi - \theta_0$; in the event that $L_z = 0$ the particle follows a polar orbit and θ covers its full range (Wilkins 1972). Turning points are given by

$$V_\theta = Q - \cot^2 \theta L_z^2 = 0. \quad (8)$$

Changing variable to $\xi = \cos^2 \theta$, we have a maximum $\xi_0 = \cos^2 \theta_0$ given by

$$\xi_0 = \frac{Q}{Q + L_z^2} = \frac{Q}{L_\infty^2}. \quad (9)$$

See Fig. 1 for a geometrical visualization. Introducing a second angular variable (Drasco & Hughes 2004)

$$\xi = \xi_0 \cos^2 \chi; \quad (10)$$

³ See Rosquist, Bylund, & Samuelsson (2009) for a discussion of the interpretation of Q in the limit $G \rightarrow 0$, corresponding to a flat spacetime.

⁴ This turning point can be found by setting the unconstrained expression for V_r equal to zero, and then solving for $E(r)$; taking the limit $r \rightarrow \infty$ gives $E \rightarrow 1$ (Wilkins 1972).

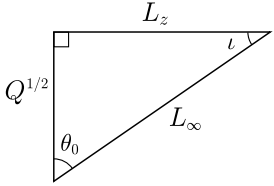


Figure 1. The angular momenta L_∞ , L_z and \sqrt{Q} define a right-angled triangle. The acute angles are θ_0 , the extremal value of the polar angle, and ι , the orbital inclination (Glampedakis, Hughes, & Kennefick 2002).

over one 2π period of χ , θ oscillates from its minimum to its maximum and back. The geodesic equation for χ is

$$(r^2 + a^2 \cos^2 \theta) \frac{d\chi}{d\tau} = \sqrt{Q + L_z^2}. \quad (11)$$

3 WAVEFORM CONSTRUCTION

We can now calculate the geodesic trajectory. The orbiting body is assumed to follow this track exactly; we ignore evolution due to the radiation of energy and angular momentum, which should be negligible for EMRBs. From this trajectory we calculate the waveform using a semirelativistic approximation (Ruffini & Sasaki 1981): we assume the particle moves along the Kerr geodesic, but radiates as if it were in flat spacetime. This quick-and-dirty technique is known as a numerical kludge (NK), and has been shown to approximate well results computed by more accurate methods (Babak et al. 2007). It is often compared to a bead travelling along a wire. The shape of the wire is set by the geodesic, but the bead moves along in flat space.

3.1 Kludge approximation

Numerical kludge approximations aim to encapsulate the main characteristics of a waveform by using the exact particle trajectory (ignoring inaccuracies from radiative effects and from the particle's self-force), whilst saving on computational time by using approximate waveform generation techniques.

We build an equivalent flat-space trajectory by identifying the Boyer-Lindquist coordinates with a set of flat-space coordinates. We consider two choices:

- (i) Identify the Boyer-Lindquist coordinates with flat-space spherical polars $\{r_{BL}, \theta_{BL}, \phi_{BL}\} \rightarrow \{r_{sph}, \theta_{sph}, \phi_{sph}\}$, then define Cartesian coordinates (Gair et al. 2005; Babak et al. 2007)

$$\mathbf{x} = \begin{pmatrix} r_{sph} \sin \theta_{sph} \cos \phi_{sph} \\ r_{sph} \sin \theta_{sph} \sin \phi_{sph} \\ r_{sph} \cos \theta_{sph} \end{pmatrix}. \quad (12)$$

- (ii) Identify the Boyer-Lindquist coordinates with flat-space oblate-spheroidal coordinates $\{r_{BL}, \theta_{BL}, \phi_{BL}\} \rightarrow \{r_{ob}, \theta_{ob}, \phi_{ob}\}$ so that the Cartesian coordinates are

$$\mathbf{x} = \begin{pmatrix} \sqrt{r_{ob}^2 + a^2} \sin \theta_{ob} \cos \phi_{ob} \\ \sqrt{r_{ob}^2 + a^2} \sin \theta_{ob} \sin \phi_{ob} \\ r_{ob} \cos \theta_{ob} \end{pmatrix}. \quad (13)$$

These are appealing because in the limit that $G \rightarrow 0$, where

the gravitating mass goes to zero, the Kerr metric in Boyer-Lindquist coordinates reduces to the Minkowski metric in oblate-spheroidal coordinates.

The two coincide for $a \rightarrow 0$ or $r \rightarrow \infty$.

There is no well motivated argument that either coordinate system must yield an accurate GW; their use is justified *post facto* by comparison with results obtained from more accurate, and computationally intensive, methods (Gair et al. 2005; Babak et al. 2007). The ambiguity in assigning flat-space coordinates reflects the inconsistency of the semirelativistic approximation: the geodesic trajectory was calculated for the Kerr geometry; by moving to flat spacetime we lose the reason for its existence. This should not be regarded as a major problem; it is an artifact of the basic assumption that the shape of the trajectory is important for determining the character of the radiation, but the curvature of the spacetime in the vicinity of the source is not. By binding the particle to the exact geodesic, we ensure that the waveform has spectral components at the correct frequencies, but by assuming flat spacetime for generation of GWs they shall not have the correct amplitudes.

3.2 Quadrupole-octupole formula

Now we have a flat-space particle trajectory $x_P^\mu(\tau)$, we may apply a flat-space wave generation formula. We use the quadrupole-octupole formula to calculate the gravitational strain (Bekenstein 1973; Press 1977; Yunes et al. 2008)

$$h^{jk}(t, \mathbf{x}) = -\frac{2G}{c^6 r} \left(\ddot{I}^{jk} - 2n_i \ddot{S}^{ijk} + n_i \dot{M}^{ijk} \right)_{t' = t - r/c}, \quad (14)$$

where an over-dot represents differentiation with respect to time t , t' is the retarded time, $r = |\mathbf{x} - \mathbf{x}_P|$ is the radial distance, \mathbf{n} is the radial unit vector, and I^{jk} , S^{ijk} and M^{ijk} are the mass quadrupole, current quadrupole and mass octupole respectively. This is correct for a slowly moving source. It is the familiar quadrupole formula (Misner, Thorne, & Wheeler 1973, section 36.10; Hobson et al. 2006, section 17.9), derived from linearized theory, plus the next order terms.

4 SIGNAL DETECTION AND ANALYSIS

4.1 The *LISA* detector

The classic *LISA* design is a three arm, space-borne laser interferometer (Bender et al. 1998; Danzmann & Rüdiger 2003). The arms form an equilateral triangle that rotates as the system's centre of mass follows a circular, heliocentric orbit, trailing 20° behind the Earth. *eLISA* has a similar design, but has only two arms, which are shorter in length, and trails 9° behind the Earth (Jennrich et al. 2011).

To describe the detector configuration, and to transform from the MBH coordinate system to those of the detector, we use three coordinate systems: those of the BH at the GC x_\bullet^i ; ecliptic coordinates centred at the solar system (SS) barycentre x_\odot^i , and coordinates that co-rotate with the detector x_d^i . The MBH's coordinate system and the SS coordinate system are depicted in Fig. 2. The mission geometry for *LISA/eLISA* is shown in Fig. 3. We define the detector coordinates such that the detector-arms lie in the x_d - y_d

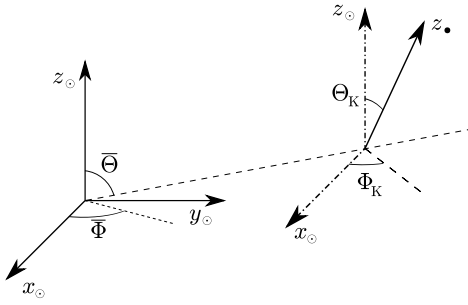


Figure 2. The relationship between the MBH's coordinate system x_\bullet^i and the SS coordinate system x_\odot^i . The MBH's spin axis is aligned with the z_\bullet -axis. The orientation of the MBH's x - and y -axes is arbitrary. We choose x_\bullet to be orthogonal to the direction to the SS.

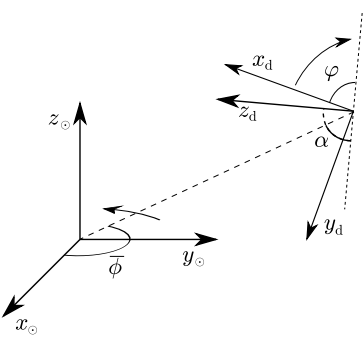


Figure 3. The relationship between the detector coordinates x_d^i and the ecliptic coordinates of the SS x_\odot^i (Bender et al. 1998; Jennrich et al. 2011). The detector inclination is $\alpha = 60^\circ$.

plane as in Cutler (1998). We have computed the waveforms in the MBH's coordinates, but it is simplest to describe the measured signal using the detector's coordinates.

The strains measured in the three arms can be combined such that *LISA* behaves as a pair of 90° interferometers at 45° to each other, with signals scaled by $\sqrt{3}/2$ (Cutler 1998). We denote the two detectors as I and II and use vector notation $\mathbf{h}(t) = (h_I(t), h_{II}(t)) = \{h_A(t)\}$ to represent signals from both detectors.

4.2 Frequency domain formalism

Having constructed the GW $\mathbf{h}(t)$ that shall be incident upon the detector, we may consider how to analyse the waveform and extract the information it contains. We briefly recap GW signal analysis, with application to *LISA*. A more complete discussion can be found in Finn (1992) and Cutler & Flanagan (1994). Adaption for *eLISA* requires a substitution of the noise distribution, and the removal of the sum over data channels, since it would only have one.

The measured strain $\mathbf{s}(t)$ is the combination of the signal and the detector noise

$$\mathbf{s}(t) = \mathbf{h}(t) + \mathbf{n}(t); \quad (15)$$

we assume the noise $n_A(t)$ is stationary and Gaussian, and that noise in the two detectors is uncorrelated, but shares the same characterisation (Cutler 1998).

The properties of the noise allow us to define a natural

inner product and associated distance on the space of signals (Cutler & Flanagan 1994)

$$(\mathbf{g}|\mathbf{k}) = 2 \int_0^\infty \frac{\tilde{g}_A(f)\tilde{k}_A(f) + \tilde{g}_A(f)\tilde{k}_A^*(f)}{S_n(f)} df, \quad (16)$$

introducing Fourier transforms

$$\tilde{g}(f) = \mathcal{F}\{g(t)\} = \int_{-\infty}^\infty g(t) \exp(2\pi ift) dt, \quad (17)$$

and $S_n(f)$ is the noise spectral density. The signal-to-noise ratio is approximately

$$\rho[\mathbf{h}] = (\mathbf{h}|\mathbf{h})^{1/2}. \quad (18)$$

The probability of a particular realization of noise $\mathbf{n}(t) = \mathbf{n}_0(t)$ is

$$p(\mathbf{n}(t) = \mathbf{n}_0(t)) \propto \exp\left[-\frac{1}{2}(\mathbf{n}_0|\mathbf{n}_0)\right]. \quad (19)$$

Thus, if the incident waveform is $\mathbf{h}(t)$, the probability of measuring signal $\mathbf{s}(t)$ is

$$p(\mathbf{s}(t)|\mathbf{h}(t)) \propto \exp\left[-\frac{1}{2}(\mathbf{s} - \mathbf{h}|\mathbf{s} - \mathbf{h})\right]. \quad (20)$$

4.3 Noise curve

LISA's noise has two sources: instrumental noise and confusion noise, primarily from white dwarf binaries. The latter may be divided into contributions from galactic and extra-galactic binaries. We use the noise model of Barack & Cutler (2004). The instrumental noise dominates at both high and low frequencies. The confusion noise is important at intermediate frequencies, and is responsible for the cusp around 10^{-3} Hz. *eLISA* shares the same sources of noise, but is less affected by confusion. Its sensitivity regime is shifted to higher frequencies because of a shorter arm length.

4.4 Window functions

There is one remaining complication regarding signal analysis: as we are Fourier transforming a finite signal we encounter spectral leakage; a contribution from large amplitude spectral components leaks into surrounding components (sidelobes), obscuring and distorting the spectrum at these frequencies (Harris 1978). This is an inherent problem with finite signals; it shall be as much of a problem when analysing signals from an actual mission as it is here. To mitigate, but unfortunately not eliminate, these effects, the time-domain signal can be multiplied by a window function. These are discussed in detail in Appendix A. We adopt the Nuttall four-term window with continuous first derivative (Nuttall 1981) for our results.

5 WAVEFORMS AND DETECTABILITY

5.1 Model parameters

The shape of the waveform depends on parameters defining the MBH; the companion object on its orbit, and the detector. Let us define $\boldsymbol{\lambda} = \{\lambda^1, \lambda^2, \dots, \lambda^Z\}$ as the set of Z parameters which specify the GW. For our model, these are:

(1) The MBH's mass M_\bullet . This is well constrained by the observation of stellar orbits about Sgr A* (Ghez et al. 2008; Gillessen et al. 2009), with best estimate $M_\bullet = (4.31 \pm 0.36) \times 10^6 M_\odot$. This depends upon the GC distance R_0 as $M_\bullet = (3.95 \pm 0.06|_{\text{stat}} \pm 0.18|_{R_0, \text{stat}} \pm 0.31|_{R_0, \text{sys}}) \times 10^6 M_\odot (R_0/8 \text{ kpc})^{2.19}$, where the errors are statistical, independent of R_0 ; statistical from the determination of R_0 , and systematic from R_0 respectively.

(2) The spin parameter a_* . Naively this could be anywhere in the range $|a_*| < 1$; however, it is possible to place an upper bound by contemplating spin-up mechanisms. Considering the torque from radiation emitted by an accretion disc, and swallowed by the BH, it can be shown that $|a_*| \lesssim 0.998$ (Thorne 1974). Magnetohydrodynamical simulations of accretion discs produce a smaller maximum value of $|a_*| \sim 0.95$ (Gammie, Shapiro, & McKinney 2004). The actual spin value could be much lower than this upper bound, depending upon the MBH's evolution.

(3, 4) The orientation angles for the MBH Θ_K and Φ_K .

(5) The ratio of the SS-GC distance R_0 and the CO mass μ , which we denote as $\zeta = R_0/\mu$. This scales the amplitude of the waveform. Bursts, unlike inspirals, do not undergo orbital evolution, hence we cannot break the degeneracy in R_0 and μ . The distance, like M_\bullet , is constrained by stellar orbits, the best estimate being $R_0 = 8.33 \pm 0.35$ kpc (Gillessen et al. 2009). The mass of the orbiting particle depends upon the type of object: whether it is an MS star, WD, NS or BH. Since we shall not know the μ precisely, we shall not be able to infer anything more about the distance.

(6, 7) The angular momentum of the CO. This can be described using either $\{L_z, Q\}$ or $\{L_\infty, \iota\}$. We employ the latter, as the total angular momentum and inclination are less tightly correlated. Assuming spherical symmetry, we expect $\cos \iota$ to be uniformly distributed.

(8–10) A set of coordinates to specify the trajectory. We use the angular phases at periape, ϕ_p and χ_p (which determines θ_p), as well as the time of periape t_p .

(11, 12) The coordinates of the MBH from the SS barycentre $\bar{\Theta}$ and $\bar{\Phi}$. These may be taken as the coordinates of Sgr A*, as the radio source is expected to be within $20r_g$ of the MBH (Reid et al. 2003; Doeleman et al. 2008). We use the J2000.0 coordinates (Reid et al. 1999; Yusef-Zadeh et al. 1999). These change with time due to the rotation of the SS about the GC; the proper motion is about 6 mas yr⁻¹, mostly in the plane of the Galaxy (Backer & Sramek 1999; Reid et al. 2003). The position is already determined to high accuracy: an EMRB can only give weak constraints on source position.⁵ We take it as known and do not try to infer it.

(13, 14) The orbital position of the detector given by $\bar{\phi}$ and φ . We assume the initial positions are chosen such that $\bar{\phi} = 0$ when $\varphi = 0$ (Cutler 1998); this choice does not qualitatively influence our results. The orbital position should be known, so need not be inferred.

We therefore have a 14 dimensional parameter space, of which we are interested in inferring $d = 10$ parameters.

⁵ For comparison, an EMRI, which should be more informative, can only give sky localisation to $\sim 10^{-3}$ steradians (Barack & Cutler 2004; Huerta & Gair 2009).

5.2 Waveforms

Figure 4 shows example waveforms to demonstrate some possible variations in the signal. All assume the standard MBH mass and position as well as a $\mu = 10M_\odot$ CO; other (randomly chosen) orbital parameters are specified in the captions. Radii are given in gravitational radii $r_g = GM_\bullet/c^2$.

The plotted waveforms use the spherical polar coordinate system for the NK. Using oblate-spheroidal coordinates makes a small difference: on the scale shown the only discernible difference would be in Fig. 4(c); the maximum difference in the waveform (outside the high-frequency tail) is $\sim 10\%$. In the other cases the difference is entirely negligible (except in the high-frequency tail, which is not of physical significance). This behaviour is typical; for the closest orbits, with the most extreme spin parameters, the maximum difference in the waveforms may be $\sim 30\%$. The difference is largely confined to the higher frequency components, which are most sensitive to the parts of the trajectory closer to the MBH: the change in flat-space radius for the same Boyer-Lindquist radial coordinate causes a slight shift in the shape of the spectrum. Enforcing the same flat-space periapse radius gives worse agreement across the spectrum.

To examine the effect of the coordinate choice, we compare SNRs calculated using the alternative schemes. The MBH parameters were fixed as for the GC, the orbital parameters were chosen such that periapse distance was drawn from a logarithmic distribution (down to the innermost stable orbit), and other parameters were drawn from appropriate uniform distributions. The ratio of the two SNRs is shown in Fig. 5. The difference from the coordinate systems is only apparent for orbits with very small periapses. There is agreement to 10% down to $r_p \simeq 4r_g$; the maximal difference may be expected to be $\sim 20\%$, this is for periapses that are only obtainable for high spin values.

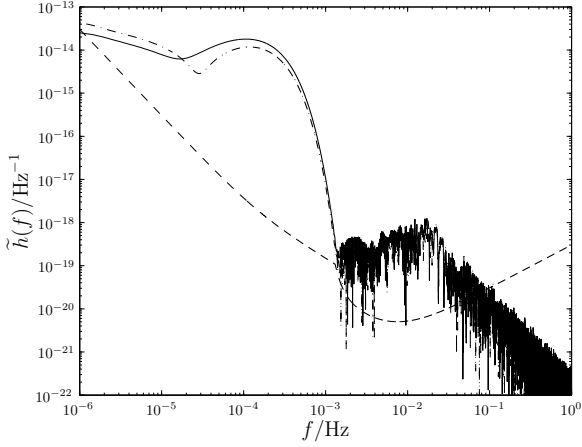
Since the deviation in the two waveforms is only apparent for small periapses, when the kludge approximation is least applicable, we conclude that the choice of coordinates is unimportant. The potential error of order 10% is no greater than that inherent in the NK approximation (see Sec. 6). Without an accurate waveform template to compare against, we do not know if there is a preferable choice of coordinates. We adopt spherical coordinates for easier comparison with existing work.

5.3 Signal-to-noise ratios

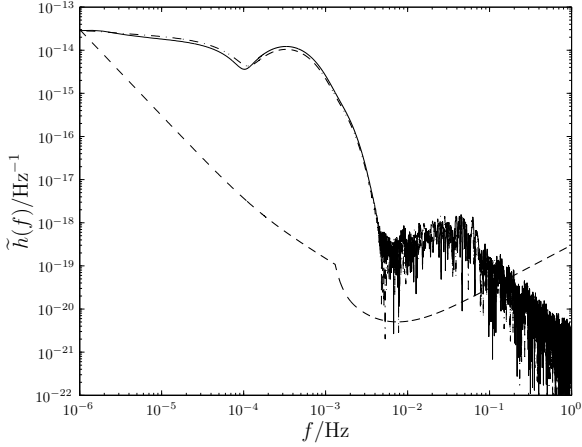
The detectability of a burst depends upon its SNR. To characterise the variation of ρ we considered a range of orbits, each for the standard MBH mass and position. These bursts were calculated for a $1M_\odot$ CO. From (14), the amplitude of the waveform is proportional to the CO mass μ and so ρ is also proportional to μ ; a $10M_\odot$ object is ten times louder on the same orbit. To make results mass independent, we use a mass-normalised SNR

$$\hat{\rho}[\mathbf{h}] = \left(\frac{\mu}{M_\odot} \right)^{-1} \rho[\mathbf{h}]. \quad (21)$$

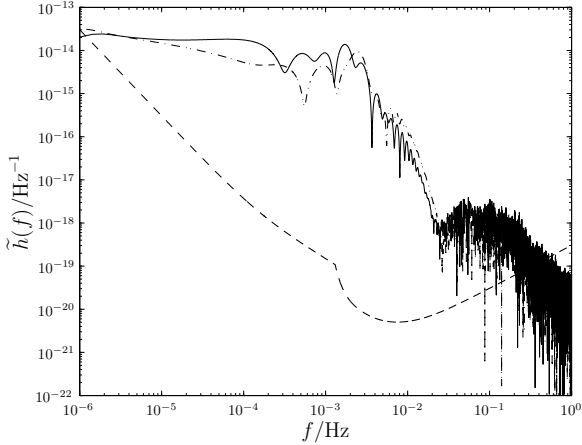
The spin of the MBH and the orbital inclination were randomly chosen, and the periapse distance was drawn from a logarithmic distribution down the inner-most stable orbit.



(a) Waveform for $a_* \simeq 0.12$, $r_p \simeq 15.6r_g$ and $\iota \simeq 2.1$. The SNR for the spherical polar kludge is $\rho[\mathbf{h}_{\text{sph}}] \simeq 451$, for the oblate-spheroidal kludge $\rho[\mathbf{h}_{\text{ob}}] \simeq 451$ (agreement to 0.01%).



(b) Waveform for $a_* \simeq 0.48$, $r_p \simeq 8.8r_g$ and $\iota \simeq 2.0$. The SNR for the spherical polar kludge is $\rho[\mathbf{h}_{\text{sph}}] \simeq 2300$, for the oblate-spheroidal kludge $\rho[\mathbf{h}_{\text{ob}}] \simeq 2310$.



(c) Waveform for $a_* \simeq 0.74$, $r_p \simeq 3.2r_g$ and $\iota \simeq 1.2$. The SNR for the spherical polar waveform is $\rho[\mathbf{h}_{\text{sph}}] \simeq 70600$, for the oblate-spheroidal kludge $\rho[\mathbf{h}_{\text{ob}}] \simeq 74900$.

Figure 4. Example burst waveforms from the GC. The strain $\tilde{h}_I(f)$ is indicated by the solid line, $\tilde{h}_{II}(f)$ by the dot-dashed line, and the noise curve by the dashed line. The kludge has been formulated using spherical polar coordinates.

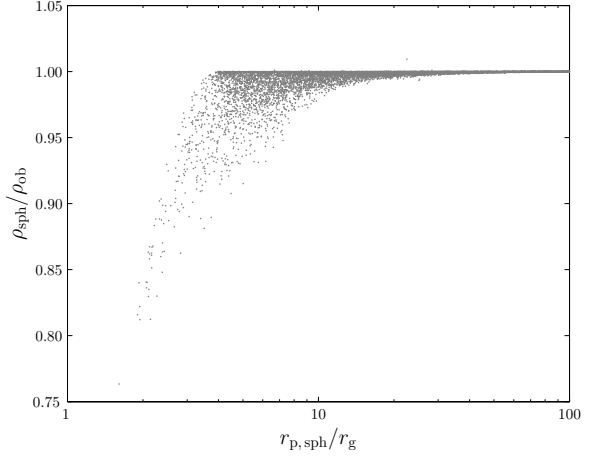


Figure 5. Ratio of the SNR for a waveform calculated using spherical polar coordinates to that for a waveform using oblate-spheroidal coordinates.

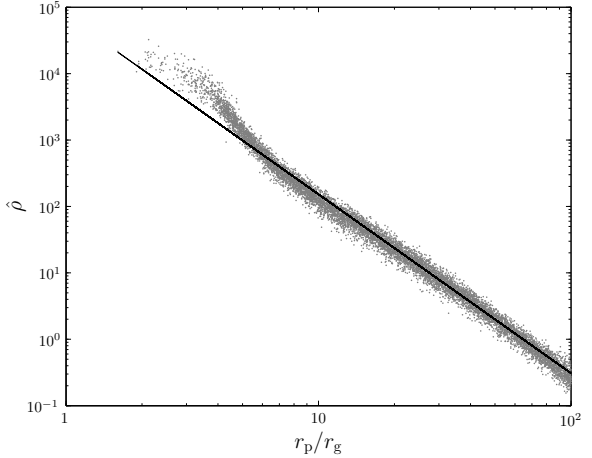


Figure 6. Mass-normalised SNR as a function of periape radius. The plotted points are the values obtained by averaging over each set of intrinsic parameters. The best fit line is $\log(\hat{\rho}) = -2.69 \log(r_p/r_g) + 4.88$. This is fitted to orbits with $r_p > 13.0r_g$ and has a reduced chi-squared value of $\chi^2/\nu = 1.73$.

For each set of these extrinsic parameters, the periape position, orientation of the MBH, and orbital position of the detector were varied: five random combinations of these intrinsic parameters (each being drawn from a separate uniform distribution) were used for each point. We take the mean of $\ln \rho$ for each set of randomised intrinsic parameters.⁶

There exists a correlation between the periape radius and SNR, as shown in Fig. 6. Closer orbits produce louder bursts. To reflect this trend, we have fitted a simple fiducial power law, indicated by the straight line.⁷ This was done by maximising the likelihood, assuming $\ln \rho$ has a Gaussian dis-

⁶ The logarithm is a better quantity to work with since the SNR is a positive-definite quantity that may be distributed over a range of magnitudes (MacKay 2003, sections 22.1, 23.3). Using median values yields results that are quantitatively similar.

⁷ Using oblate-spheroidal coordinates instead of spherical polars gives a fit consistent to within 0.1% as we have excluded the closest orbits.

tribution with standard deviation derived from the scatter because of variation in the intrinsic parameters. The power law is a good fit only for larger periapses. The shape is predominately determined by the noise curve. The change in the trend reflects the transition as from approximately power law behaviour to the bucket of the noise curve. Hence, we fit a power law to orbits with a characteristic frequency of $f_* = \sqrt{GM_\bullet/r_p} < 1 \times 10^{-3}$ Hz, to avoid spilling into the bucket. Changing the cut-off within a plausible region alters the fit coefficients by around 0.1.⁸

The SNR shows no clear correlation with the other parameters (excluding μ). However, the SNR is sensitive to the intrinsic parameters, in particular the initial position, and may vary by an order of magnitude.

Setting a threshold of $\rho = 10$, a $1M_\odot$ ($10M_\odot$) object would be expected to be detectable if the periapse distance is less than $27r_g$ ($65r_g$). Hopman et al. (2007), assuming a threshold of $\rho = 5$, used an approximate form for the SNR based upon the quadrupole component of a circular orbit; their model, with updated parameters for the MBH, predicts bursts would be detectable out to $66r_g$ ($135r_g$). This is overly optimistic.

6 ENERGY SPECTRA

To check the NK waveforms, we compare the energy spectra calculated from these with those obtained from the classic treatment of Peters & Mathews (1963) and Peters (1964). This calculates GW emission for Keplerian orbits in flat spacetime, assuming only quadrupole radiation. The spectrum produced should be similar to that obtained from the NK in weak fields, that is for large periapses; we do not expect an exact match because of the differing input physics and varying approximations.

In addition to using the energy spectrum, we also use the total energy flux. This contains less information than the spectrum; however, results have been calculated for parabolic orbits in Schwarzschild spacetime using time-domain black hole perturbation theory (Martel 2004). These should be more accurate than results calculated using the Peters and Mathews formalism.

We do not intend to use the kludge waveforms to calculate an accurate energy flux: this would be inconsistent as we assume the orbits do not evolve with time. We only calculate the energy flux as a sanity check, to confirm that the kludge approximation is consistent with other approaches.

6.1 Kludge spectrum

A gravitational wave in the TT gauge has an effective energy-momentum tensor (Misner et al. 1973, section 35.15)

$$T_{\mu\nu} = \frac{c^4}{32\pi G} \left\langle \partial_\mu h_{ij} \partial_\nu h^{ij} \right\rangle, \quad (22)$$

⁸ The power law exponent -2.7 is inconsistent with $-13/4$ as predicted by the approximate model of Hopman et al. (2007). This is the result of their approximate waveform model.

where $\langle \dots \rangle$ indicates averaging over several wavelengths or periods. The energy flux through a sphere of radius R is

$$\frac{dE}{dt} = \frac{c^3}{32\pi G} R^2 \int d\Omega \left\langle \frac{dh_{ij}}{dt} \frac{dh^{ij}}{dt} \right\rangle, \quad (23)$$

with $\int d\Omega$ representing integration over all solid angles. From (14) the waves have a $1/r$ dependence; if we define

$$h_{ij} = \frac{H_{ij}}{r}, \quad (24)$$

we see, the flux is independent of R , as required for energy conservation, and

$$\frac{dE}{dt} = \frac{c^3}{32\pi G} \int d\Omega \left\langle \frac{dH_{ij}}{dt} \frac{dH^{ij}}{dt} \right\rangle. \quad (25)$$

Integrating to find the total energy emitted we obtain

$$E = \frac{c^3}{32\pi G} \int d\Omega \int_{-\infty}^{\infty} dt \frac{dH_{ij}}{dt} \frac{dH^{ij}}{dt}. \quad (26)$$

Since we are considering all time, the localization of the energy is no longer of importance and it is unnecessary to average over several periods. Switching to Fourier representation $\tilde{H}_{ij}(f) = \mathcal{F}\{H_{ij}(t)\}$,

$$E = \frac{\pi c^3}{4G} \int d\Omega \int_0^{\infty} df f^2 \tilde{H}^{ij}(f) \tilde{H}_{ij}^*(f), \quad (27)$$

using $\tilde{H}_{ij}^*(f) = \tilde{H}_{ij}(-f)$ as the signal is real. From this we identify the energy spectrum as

$$\frac{dE}{df} = \frac{\pi c^3}{4G} \int d\Omega f^2 \tilde{H}^{ij}(f) \tilde{H}_{ij}^*(f). \quad (28)$$

6.2 Peters and Mathews spectrum

To calculate the Peters and Mathews energy spectrum for a parabolic orbit, we use the limiting result of Turner (1977). This result should be accurate to $\sim 10\%$ for orbits with periapse radii larger than $\sim 20r_g$ (Berry & Gair 2010).

6.3 Comparison

Two energy spectra are plotted in Fig. 7 for orbits with periapses of $r_p = 15.0r_g$, $30.0r_g$ and $60.0r_g$. The two spectra appear to be in good agreement, showing the same general shape in the weak-field limit. The NK spectrum is more tightly peaked, but is always within a factor of 2 at the apex. The peak of the spectrum is shifted to a marginally higher frequency in the NK spectrum primarily because of the addition of the higher order terms.

Comparing the total energy fluxes, ratios of the various energies are plotted in Fig. 8. We introduce an additional energy, the quadrupole NK energy $E_{NK(Q)}$. This allows easier comparison with the Peters and Mathews energy which includes only quadrupole radiation. It can be calculated in three ways:

- (i) Inserting the waveform $\tilde{h}(f)$ generated including only the mass quadrupole term in (14) into (27) and integrating. This is equivalent to the method used to calculate E_{NK} .

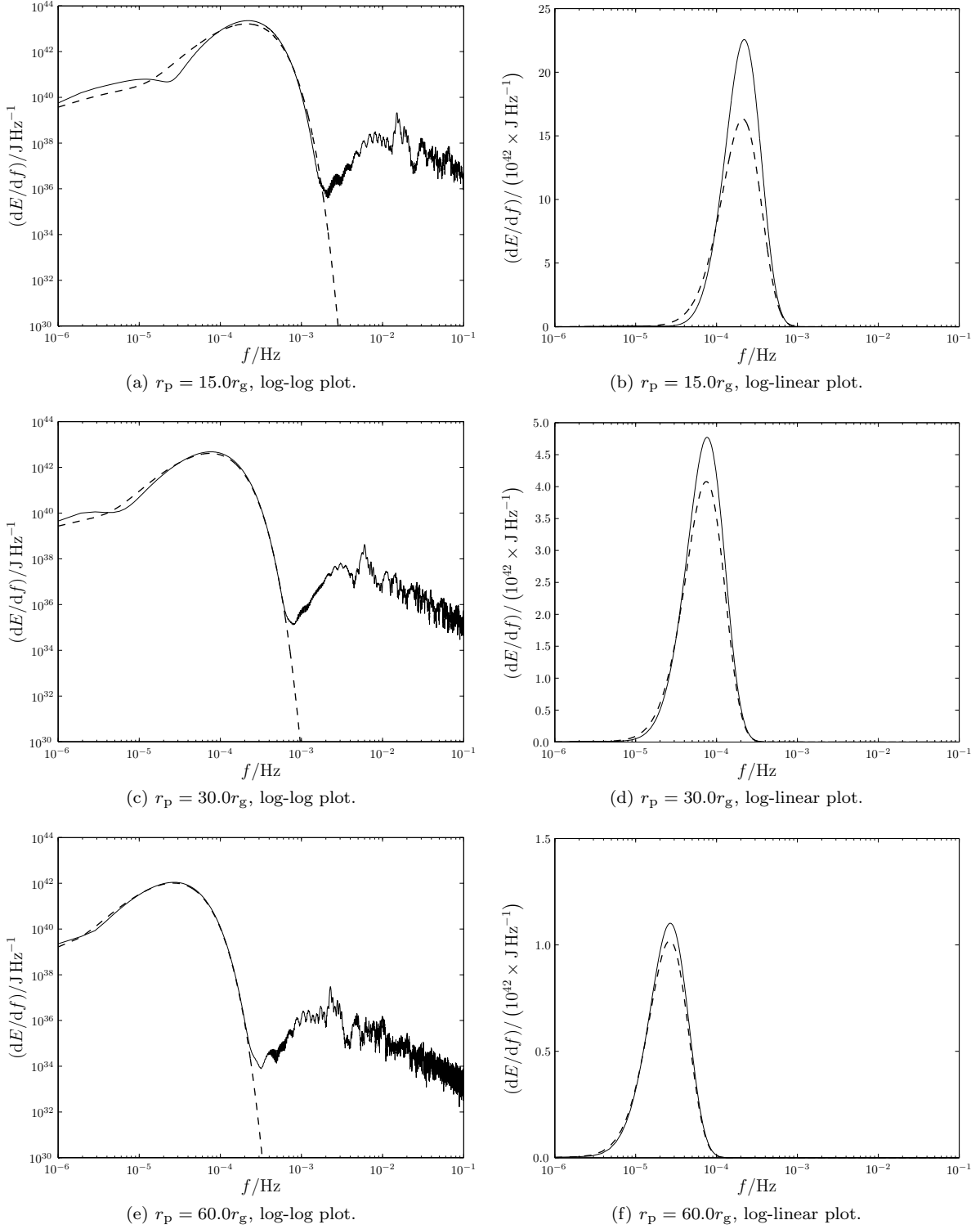


Figure 7. Energy spectra for a parabolic orbit of a $\mu = 10M_\odot$ object about a Schwarzschild BH with $M_\bullet = 4.31 \times 10^6 M_\odot$. The spectra calculated from the NK waveform are shown by the solid line and the Peters and Mathews flux is indicated by the dashed line. The NK waveform includes current quadrupole and mass octupole contributions. The high frequency tail is the result of spectral leakage.

(ii) Numerically integrating the quadrupole GW luminosity (Misner et al. 1973, section 36.7; Hobson et al. 2006, section 18.7)

$$E = \frac{G}{5c^9} \int \ddot{\mathcal{I}}_{ij} \ddot{\mathcal{I}}^{ij} dt, \quad (29)$$

where $\mathcal{I}_{ij} = I_{ij} - (1/3)I\delta_{ij}$ is the reduced mass quadrupole tensor. We can obtain this from (26), by integrating over all angles when the waveform only contains the mass quadrupole component. This has the advantage of avoid-

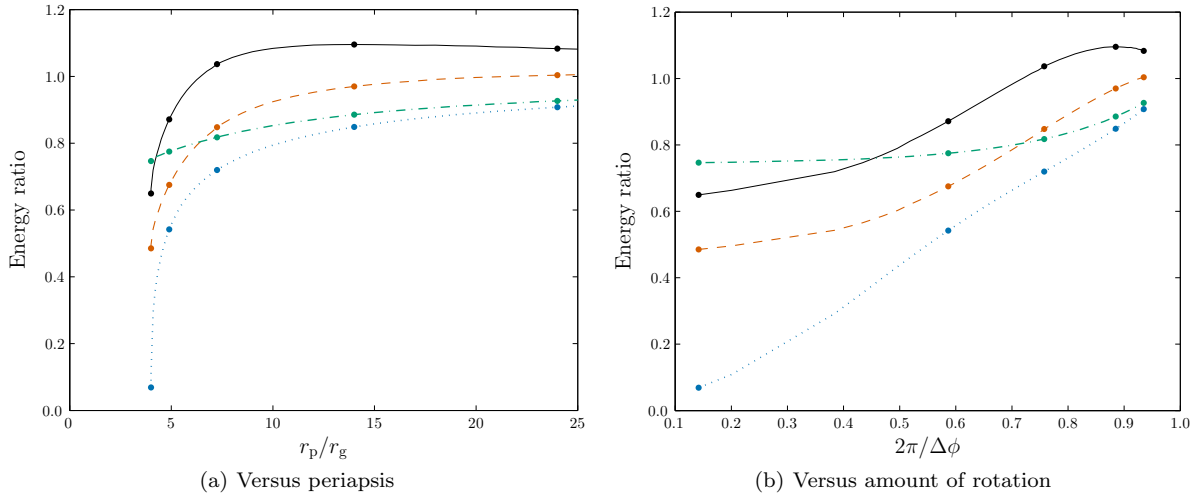


Figure 8. Ratios of energies as a function of periapsis r_p and 2π divided by the total angle of rotation in one orbit $\Delta\phi$ ($2\pi/\Delta\phi = 1$ for a Keplerian orbit). The solid line shows the ratio of the numerical kludge and Martel energies E_{NK}/E_M ; the dashed line shows the ratio of the NK energy calculated using only the mass quadrupole term and the Martel energy $E_{NK(Q)}/E_M$; the dot-dashed line shows the ratio of the quadrupole and quadrupole-octupole NK energies $E_{NK(Q)}/E_{NK}$, and the dotted line shows the ratio of the Peters and Mathews and quadrupole NK energies $E_{PM}/E_{NK(Q)}$. The spots show the mapping between the two abscissa scales. Compare with figure 4 of Gair et al. (2005).

ing the effects of spectral leakage or the influence of window functions.

(iii) Using the analytic expressions for the integral (29) given in appendix A of Gair et al. (2005).

All three agree to within computational error. No difference is visible on the scale plotted in Fig. 8. This demonstrates the validity of the code, and shows that the use of a window function does not significantly distort the waveform.

The ratios all tend towards one in the weak field, as required, but differences become more pronounced in the strong field. The NK energy is larger than the Peters and Mathews result E_{PM} . This behaviour has been seen before for high eccentricity orbits about a non-spinning BH (Gair et al. 2005). It may be explained by considering the total path length for the different orbits: the Peters and Mathews spectrum assumes a Keplerian orbit, the orbit in Kerr geometry rotates more than this. The greater path length leads to increased emission of gravitational waves and a larger energy flux (Berry & Gair 2010). Our bead must travel further along its wire. A good proxy for the path length is the angle of rotation $\Delta\phi$; this is 2π for a Keplerian orbit, in Kerr the angle should be 2π in the limit of an infinite periapsis, whereas for a periapsis small enough that the orbit shows zoom-whirl behaviour, the total angle may be many times 2π . There is a reasonable correlation between the amount of rotation $2\pi/\Delta\phi$ and the ratio of energies.

Error in the NK energy compared with the time-domain black hole perturbation theory results of Martel comes from two sources: the neglecting of higher order multipole contributions and the ignoring of background curvature. The contribution of the former can be estimated by looking at the difference in the NK energy by including the current quadrupole and mass octupole terms. From Fig. 8 we see these terms give a negligible contribution in the weak field, but the difference is $\sim 20\%$ in the strong field. This explains why the Martel energy E_M is greater in the strong

field: it includes contributions from all multipoles. Neglecting the background curvature increases the NK energy relative to E_M . This partially cancels out the error introduced by not including higher order terms: this accidentally leads to $E_{NK(Q)}$ being more accurate than E_{NK} for $r_p \gtrsim 10r_g$ (Tanaka et al. 1993).

From the level of agreement we may be confident that the NK waveforms are a reasonable approximation. The difference in energy flux is only greater than 10% for very strong fields $r_p \simeq 4r_g$; since this is dependent on the square of the waveform, typical accuracy in the waveform may be $\sim 5\%$ (Gair et al. 2005; Tanaka et al. 1993). This is more significant than the variation in waveforms we generally found using the two alternative coordinate systems for the NK (in this case the two coincide because $a_* = 0$).

7 PARAMETER ESTIMATION

Having detected a signal, we are interested in what we can learn about the source. We have an inference problem that can be solved by application of Bayes' Theorem (Jaynes 2003, chapter 4): the probability distribution for our parameters given that we have detected the signal $\mathbf{s}(t)$ is given by the posterior

$$p(\boldsymbol{\lambda}|\mathbf{s}(t)) = \frac{p(\mathbf{s}(t)|\boldsymbol{\lambda})p(\boldsymbol{\lambda})}{p(\mathbf{s}(t))}. \quad (30)$$

Here $p(\mathbf{s}(t)|\boldsymbol{\lambda})$ is the likelihood of the parameters, $p(\boldsymbol{\lambda})$ is the prior probability distribution for the parameters, and the evidence $p(\mathbf{s}(t)) = \int p(\mathbf{s}(t)|\boldsymbol{\lambda}) d^d\lambda$ is, for our purposes, a normalising constant. The likelihood depends upon the realization of noise. If parameters $\boldsymbol{\lambda}_0$ define a waveform $\mathbf{h}_0(t) = \mathbf{h}(t; \boldsymbol{\lambda}_0)$, the probability that we observe signal $\mathbf{s}(t)$ GW is given by (20), so the likelihood is

$$p(\mathbf{s}(t)|\boldsymbol{\lambda}_0) \propto \exp \left[-\frac{1}{2} (\mathbf{s} - \mathbf{h}_0 | \mathbf{s} - \mathbf{h}_0) \right]. \quad (31)$$

If we were to define this as a probability distribution for the parameters $\boldsymbol{\lambda}$, the modal values are the maximum-likelihood (ML) parameters $\boldsymbol{\lambda}_{\text{ML}}$. The waveform $\mathbf{h}(t; \boldsymbol{\lambda}_{\text{ML}})$ is the signal closest to $\mathbf{s}(t)$, where distance is defined using the inner product (16) (Cutler & Flanagan 1994).

7.1 Fisher matrices

In the limit of a high SNR, we may approximate (Vallisneri 2008)

$$p(\mathbf{s}(t)|\boldsymbol{\lambda}_0) \propto \exp \left[-\frac{1}{2} (\partial_a \mathbf{h} | \partial_b \mathbf{h}) (\lambda^a - \langle \lambda^a \rangle_\ell) (\lambda^b - \langle \lambda^b \rangle_\ell) \right], \quad (32)$$

where the mean is defined as

$$\langle \lambda^a \rangle_\ell = \frac{\int \lambda^a p(\mathbf{s}(t)|\boldsymbol{\lambda}) d^d \lambda}{\int p(\mathbf{s}(t)|\boldsymbol{\lambda}) d^d \lambda}. \quad (33)$$

In the high SNR limit, this is the ML value $\langle \lambda^a \rangle_\ell = \lambda_{\text{ML}}^a$. The quantity

$$\Gamma_{ab} = (\partial_a \mathbf{h} | \partial_b \mathbf{h}) \quad (34)$$

is the Fisher information matrix (FIM). It controls the variance of the likelihood distribution.

The form of the posterior distribution depends upon the nature of the prior information. If we have an uninformative prior, such that $p(\boldsymbol{\lambda})$ is a constant, the posterior distribution is determined by the likelihood. In the high SNR limit, we obtain a Gaussian with variance-covariance matrix

$$\boldsymbol{\Sigma} = \boldsymbol{\Gamma}^{-1}. \quad (35)$$

The FIM therefore gives the uncertainty associated with the inferred parameters, in this case the ML values.

If the prior restricts the allowed range for a parameter, as is the case for the spin a_* , then the posterior is a truncated Gaussian, and $\boldsymbol{\Gamma}^{-1}$ may no longer represent the variance-covariance.

If the prior is approximately Gaussian with variance-covariance matrix $\boldsymbol{\Sigma}_0$, the posterior is also Gaussian.⁹ The posterior variance-covariance is (Cutler & Flanagan 1994; Vallisneri 2008)

$$\boldsymbol{\Sigma} = (\boldsymbol{\Gamma} + \boldsymbol{\Sigma}_0^{-1})^{-1}. \quad (36)$$

From this the inverse FIM $\boldsymbol{\Gamma}^{-1}$ is an upper bound on the size of the posterior covariance matrix.¹⁰

The FIM gives a quick way of estimating the range of the posterior. It is widely used because of this. However, it is only appropriate when the approximation of (32) holds. This is known as the linearised-signal approximation (LSA), where higher order derivatives are neglected. To assess the

⁹ If we only know the typical value and spread of a parameter, a Gaussian is the maximum entropy prior (Jaynes 2003, section 7.11): the prior that is least informative given what we know.

¹⁰ It is also the Cramér-Rao bound on the error covariance of an unbiased estimator (Cutler & Flanagan 1994; Vallisneri 2008). Thus it represents the frequentist error: the lower bound on the covariance for an unbiased parameter estimator $\boldsymbol{\lambda}_{\text{est}}$ calculated from an infinite set of experiments with the same signal $\mathbf{h}(t)$ but different realisations of the noise $\mathbf{n}(t)$.

validity of this, Vallisneri (2008) recommends use of the maximum-mismatch (MM) criterion

$$\ln r = -\frac{1}{2} (\Delta \lambda^a \partial_a \mathbf{h}_{\text{ML}} - \Delta \mathbf{h} | \Delta \lambda^b \partial_b \mathbf{h}_{\text{ML}} - \Delta \mathbf{h}). \quad (37)$$

Here $\Delta \boldsymbol{\lambda}$ is the displacement to some point on the 1σ surface

$$\Delta \boldsymbol{\lambda} = \boldsymbol{\lambda}_{1\sigma} - \boldsymbol{\lambda}_{\text{ML}}, \quad (38)$$

and $\Delta \mathbf{h}$ is the corresponding change in the waveform

$$\Delta \mathbf{h} = \mathbf{h}(\boldsymbol{\lambda}_{1\sigma}) - \mathbf{h}(\boldsymbol{\lambda}_{\text{ML}}). \quad (39)$$

The 1σ surface is defined from the inverse of the FIM. If higher order terms are indeed negligible, the MM criterion is small. We check this by picking a random selection of points on the 1σ surface and evaluating $|\ln r|$. If this is smaller than a fiducial value ($|\ln r| = 0.1$) over the majority (90%) of the surface we consider the LSA sufficiently justified.

We calculated FIMs for a wide range of orbits and checked the MM criterion. We found that for the overwhelming majority the test failed: the LSA is not appropriate. This behaviour was seen even for orbits with $\rho \sim 10^3 - 10^4$.¹¹ Higher order terms are important, and cannot be neglected.

EMRBs have a short duration and accordingly are not the most informative of signals. Therefore, the 1σ surface as defined by considering only the LSA terms is large. Taking such a step in parameter space moves the signal beyond the region of linear changes.

We hope that this shall serve as an example to others. What constitutes high SNR depends upon the signal; it is not enough for $\rho > 1$. As stressed by Vallisneri (2008), it is essential to check the MM criterion for individual waveforms: the threshold for the LSA to become applicable could be much greater than naively thought.

As we cannot be confident in FIM results, we abandon this approach in favour of using Markov chain Monte Carlo simulations to explore constraints from different regions of parameter space. These are computationally more expensive, but do not rely on any approximations.

7.2 Markov chain Monte Carlo methods

Markov chain Monte Carlo (MCMC) methods are widely used for inference problems; they are a family of algorithms for integrating over complicated distributions and are efficient for high-dimensional problems (MacKay 2003, chapter 29). Parameter space is explored by constructing a chain of N samples. The distribution of points visited by the chain maps out the underlying distribution; this becomes asymptotically exact as $N \rightarrow \infty$. Samples are added sequentially, if the current state is $\boldsymbol{\lambda}_n$ a new point $\boldsymbol{\lambda}^*$ is drawn and accepted with probability

$$\mathcal{A} = \min \left\{ \frac{\pi(\boldsymbol{\lambda}^*) \mathcal{L}(\boldsymbol{\lambda}^*) \mathcal{Q}(\boldsymbol{\lambda}_n; \boldsymbol{\lambda}^*)}{\pi(\boldsymbol{\lambda}_n) \mathcal{L}(\boldsymbol{\lambda}_n) \mathcal{Q}(\boldsymbol{\lambda}_n; \boldsymbol{\lambda}^*)}, 1 \right\}, \quad (40)$$

setting $\boldsymbol{\lambda}_{n+1} = \boldsymbol{\lambda}^*$, where $\mathcal{L}(\boldsymbol{\lambda})$ is the likelihood, in our case from (31); $\pi(\boldsymbol{\lambda})$ is the prior, and \mathcal{Q} is a proposal distribution. If the move is not accepted $\boldsymbol{\lambda}_{n+1} = \boldsymbol{\lambda}_n$. This is

¹¹ In this study, to increase ρ we must reduce the periape distance; this also reduces the region where the LSA is valid as parameter dependencies become more non-linear. If we had the luxury of increasing ρ by moving the GC closer, things could be different.

the Metropolis-Hastings algorithm (Metropolis et al. 1953; Hastings 1970).

Waiting long enough yields an exact posterior, but it is desirable for the MCMC to converge quickly. This requires a suitable choice for the proposal distribution, which can be difficult, since we do not yet know the shape of the target distribution.

One method to define the proposal is to use the previous results in the chain and refine \mathcal{Q} by learning from these. Such approaches are known as adaptive methods. Updating using previous points means that the chain is no longer Markovian. Care must be taken to ensure that ergodicity is preserved and convergence obtained (Roberts & Rosenthal 2007; Andrieu & Thoms 2008). To avoid this complication, we follow Haario et al. (1999), and use the adapting method as a burn in phase. We have an initial phase where the proposal is updated based upon accepted points. After this we fix the proposal and proceed as for a standard MCMC. By only using samples from the second part, we guarantee that the chain is Markovian and ergodic, whilst still enjoying the benefits of a tailor-made proposal. After only a finite number of samples we cannot assess the optimality of this (Andrieu & Thoms 2008), but the method is still effective.

To tune \mathcal{Q} , we use an approach based upon the adaptive Metropolis algorithm (Haario et al. 2001). The proposal is taken to be a multivariate normal distribution centred upon the current point, the covariance of which is

$$\mathbf{C} = s(\mathbf{V}_n + \varepsilon\mathbf{C}_0), \quad (41)$$

where \mathbf{V}_n is the covariance of the accepted points $\{\boldsymbol{\lambda}_1, \dots, \boldsymbol{\lambda}_n\}$, s is a scaling factor that controls the step size, ε is a small positive constant (typically 0.0025), and \mathbf{C}_0 is a constant matrix included to ensure ergodicity.

Our adaptation is run in three phases. The initial phase is to get the chain moving. For this $\mathbf{C}_0^{\text{init}}$ is a diagonal matrix with elements calibrated from initial one dimensional MCMCs. This finishes after N_{init} accepted points.

For the second phase, we use the proposal covariance from the initial phase \mathbf{C}^{init} for $\mathbf{C}_0^{\text{main}}$. We reset the covariance of the accepted points so that it only includes points from this phase. This is the main adaptation phase and lasts until N_{main} points have been accepted.

In the final adaptation phase we restart the chain at the true parameter values. We no longer update the shape of the covariance (\mathbf{V}_n remains fixed), but adjust the step size s to tune the acceptance rate; it is then fixed, along with everything else, for the final MCMC.

Throughout the adaptation, we update the step size s after every 100 trial points (whether or not they are accepted). While updating, the covariance \mathbf{V}_n changes after every 1000 trial points. We set $N_{\text{init}} = 50000$ and $N_{\text{main}} = 450000$.

We initially aimed for an acceptance rate of 0.234; this is optimal for a random walk Metropolis algorithm with some specific high-dimensional target distributions (Roberts et al. 1997; Roberts & Rosenthal 2001). In many cases we found better convergence when aiming for a lower acceptance rate, say 0.1. This is not unexpected: the optimal rate may be lower than 0.234 when the parameters are not independent and identically distributed (Bédard 2007, 2008b,a). In practice, the final acceptance rate is (almost always)

lower than the target rate as the use of a multivariate Gaussian for the proposal distribution is rarely a good fit at the edges of the posterior. Consequently, the precise choice for the target acceptance rate is unimportant as long as it is of the correct magnitude. Final rates are typically within a factor of 2 of the target value. As an initial choice, we set $s = 2.38^2/d$, which is the optimal choice if \mathbf{C} was the true target covariance for a high dimensional target of independent and identically distributed parameters (Gelman et al. 1996; Roberts et al. 1997; Roberts & Rosenthal 2001; Haario et al. 2001).¹²

To assess the convergence of the MCMC we check the trace plot (the parameters values throughout the run) for proper mixing, that the one and two dimensional posterior plots fill out to a smooth distribution, and that the distribution widths tend towards consistent values.

8 RESULTS

8.1 Data set

To investigate the information contained in EMRBs, we again considered a range of orbits. The MBH was assumed to have the standard mass and position. The CO was chosen to be $10M_\odot$, as the most promising candidates for EMRBs would be BHs: they are massive and hence produce higher SNR bursts, they are more likely to be on close orbits as a consequence of mass segregation (Bahcall & Wolf 1977; Alexander & Hopman 2009; Pretor & Amaro-Seoane 2010; Amaro-Seoane & Pretor 2011), and they cannot be tidally disrupted.

Other potential source candidates would be NSs and low mass MS stars. Like BHs, NSs are not tidally disrupted in the GC, and benefit (albeit weakly) from mass segregation. MS stars have the great advantage of being more numerous than stellar remnants. Most MS stars would be tidally disrupted at periapses of interest, but the lowest mass stars could be viable sources (Freitag 2003; Amaro-Seoane 2012).¹³ These could produce more intricate waveforms, since they are extended bodies, subject to tidal distortion, rather than point masses. We stick to BHs as the most credible and simplest source. Modelling extended bodies is left for future work.

Orbits were chosen with periapses uniformly distributed in logarithmic space between the inner-most orbit and $16r_g$. The other parameters were chosen randomly from appropriate uniform distributions.

The results of the MCMC runs illustrate why the FIM approach was insufficient. There are strong and complex parameter dependencies. For many sets of parameters the posteriors are far from Gaussian as assumed in the LSA. Some example results are shown in Fig. 9, 10 and 11.

The first is well-behaved. It is almost Gaussian, but we see some asymmetries and imperfections. There are also strong degeneracies, indicated by needle-like distributions.

¹² Reasonably good results may be obtained by fixing s at this value, and not adjusting to fine tune the acceptance rate.

¹³ The optimal density to resist disruption occurs at $\mu \simeq 0.07M_\odot$ (Chabrier & Baraffe 2000). Bursts for these objects should be detectable if $r_p \lesssim 10r_g$.

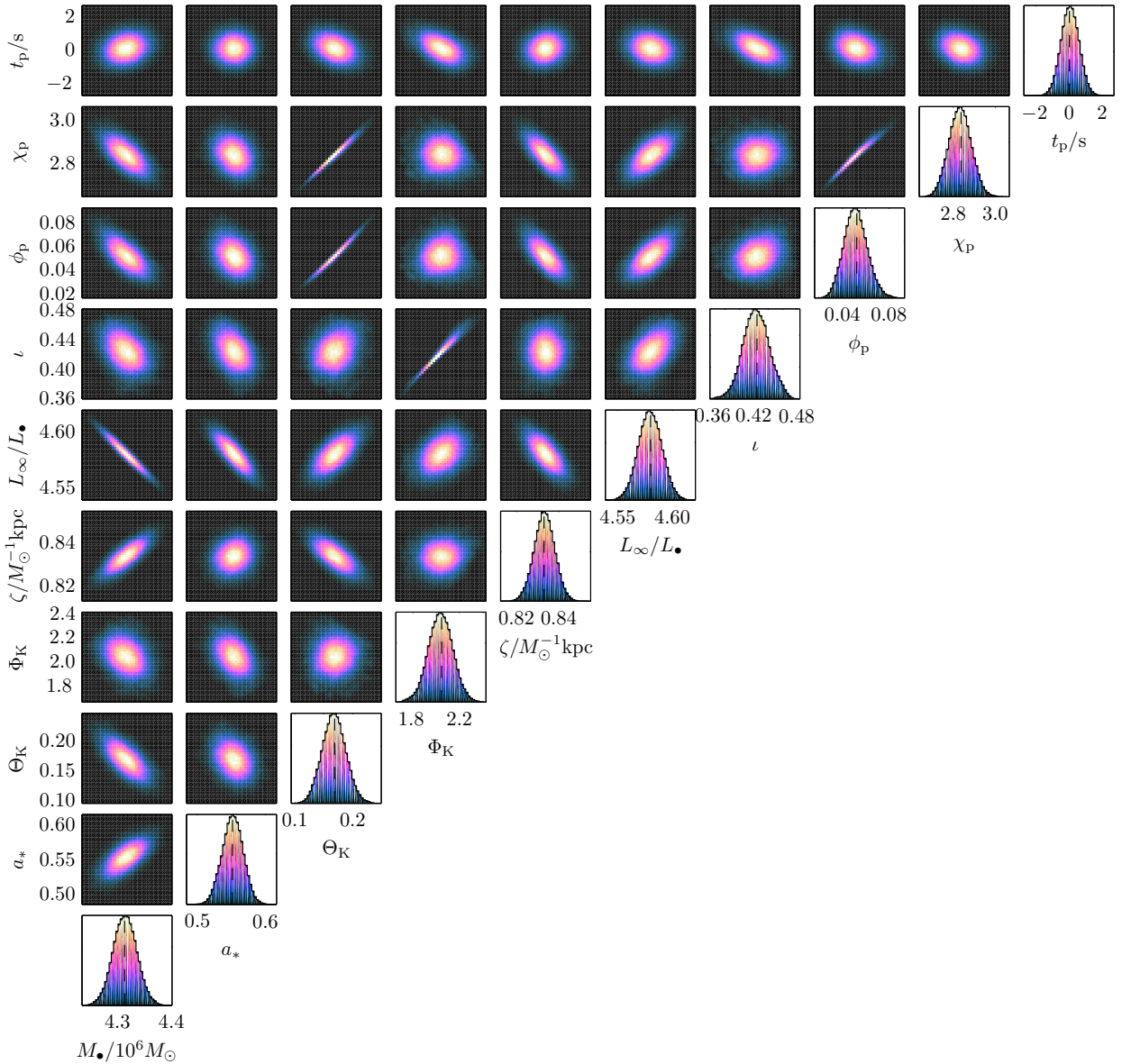


Figure 9. Marginalised one and two dimensional posteriors. The scales are identical in both sets of plots. The dotted line indicates the true value. These distributions are fairly cromulent and well converged. Angular momentum is in units of $L_\bullet = GM_\bullet c^{-1}$. The input orbit has $r_p \simeq 8.54r_g$ and $\rho \simeq 916$.

This is a fairly standard example: there are runs which are closer to being Gaussian (especially at higher SNR), and equally there are tighter degeneracies. The lenticular $M_\bullet - L_\infty$ degeneracy is common.

The second shows banana-like degeneracies. These are not uncommon; there are varying degrees of curvature. The more complicated shape makes it harder for the MCMC to converge, so the final distribution is not as smooth as for the first example. The curving degeneracies also bias the one dimensional marginalisations away from the true values.

The third shows more intricate behaviour. This is more rare, but indicates the variety of shapes that is obtainable. Again the convergence is more difficult, so the distributions are rougher around the edges; there is also some biasing due to the curving degeneracies.

These results do not incorporate any priors (save to

keep them within realistic ranges); we have not folded in the existing information we have, for example, about the MBH's mass. Therefore, the resulting distributions characterise what we could learn from EMRBs alone. By the time a space-borne GW detector finally flies, we will have much better constraints on some parameters.

It is possible to place good constraints from the closest orbits. These can provide sufficient information to give beautifully behaved posteriors although significant correlation between parameters persists.

8.2 Distribution widths

Characteristic distribution widths are shown in Fig. 12. Plotted are the standard deviation σ_{SD} ; a scaled 50-percentile range $\sigma_{50} = W_{50}/1.34898$, where W_{50} is the range

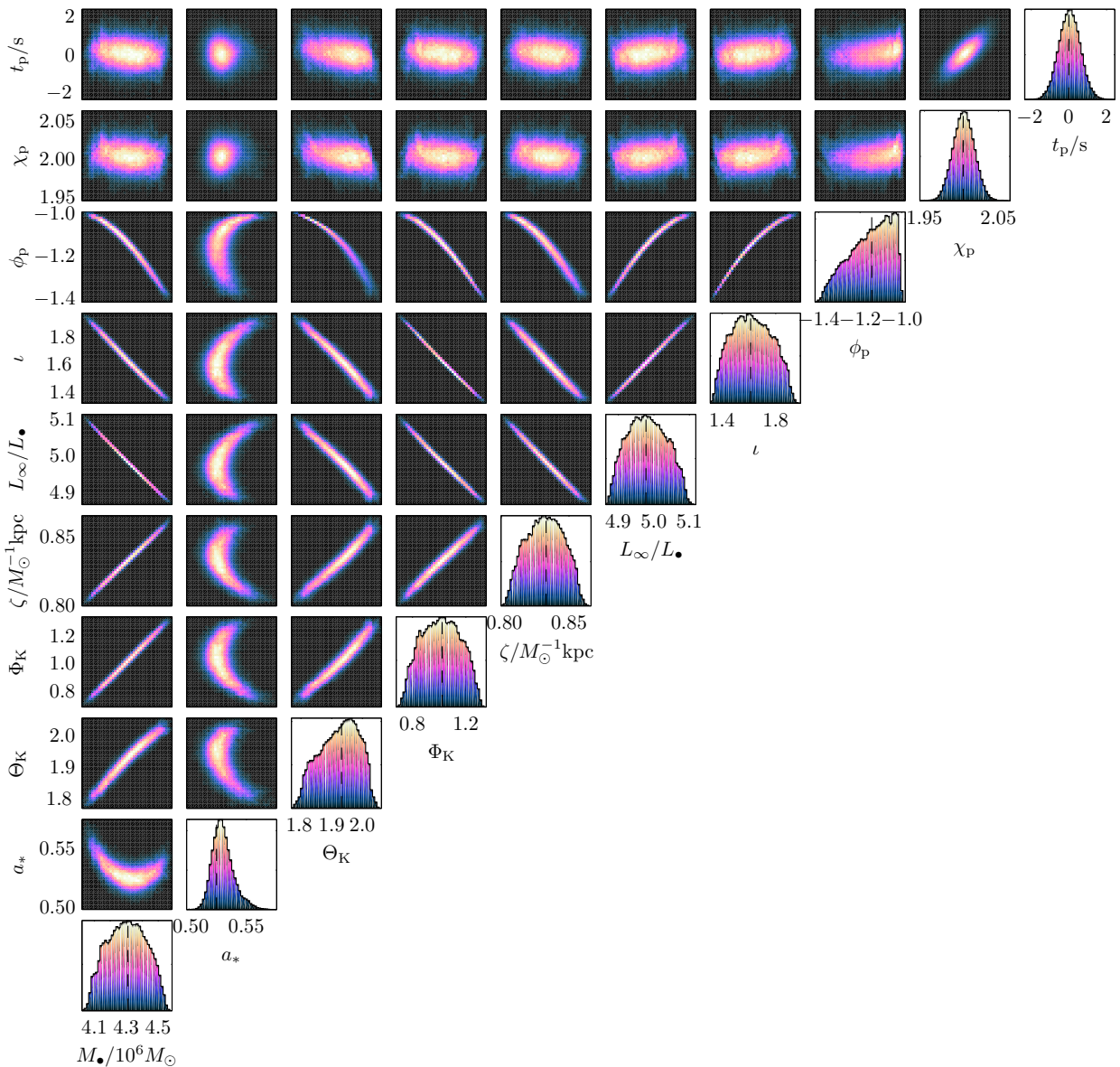


Figure 10. Marginalised one and two dimensional posteriors. The scales are identical in both sets of plots. The dotted line indicates the true value. These distributions show definite non-gaussianity. The input orbit has $r_p \simeq 9.86r_g$ and $\rho \simeq 1790$.

that contains the median 50% of points, and a scaled 95-percentile range $\sigma_{95} = W_{95}/3.919928$, where W_{95} is the 95% range. These widths are equal for a normal distribution. Filled circles are used for runs that appear to have converged. Open circles are for those yet to converge, but which appear to be approaching an equilibrium state; widths should be accurate to within a factor of a few. For guidance, the dotted line corresponds to the current measurement uncertainty for M_\bullet ; the dashed lines are from uniform priors for a_* , Φ_K , ϕ_p , χ_p , $\cos\Theta_K$ and $\cos\iota$, and, for completeness, the solid line indicates the total prior range. We have no expectations for the width of the MBH mass distribution with respect to the current value; however, we would expect that the recovered distributions for the other parameters are narrower than for the case of complete ignorance. This may not be the case if the distribution is multimodal: in this event using the width is an inadequate description of the distribution.

Only a few unconverged runs exceed these limits, and some appear to be multimodal.

The widths show a trend of decreasing with decreasing periaxis or increasing SNR, but there is a large degree of scatter. There does not appear to be a strong dependence upon any single input parameter, with the exception of the spin. The widths for ι , Θ_K , Φ_K , ϕ_p and χ_p increase for smaller spin magnitudes. The dependence is shown in Fig. 13. These parameters are defined with reference to the coordinate system established by the spin axis: for $a_* = 0$ we have spherical symmetry and there would be ambiguity in defining them. Therefore, it makes sense that they can be more accurately determined for larger spin magnitudes. The width for a_* , however, shows no clear correlation.

Comparing our MCMC and FIM results, we see there can be significant differences. Most parameters give results consistent to within an order (or two) of magnitude. The

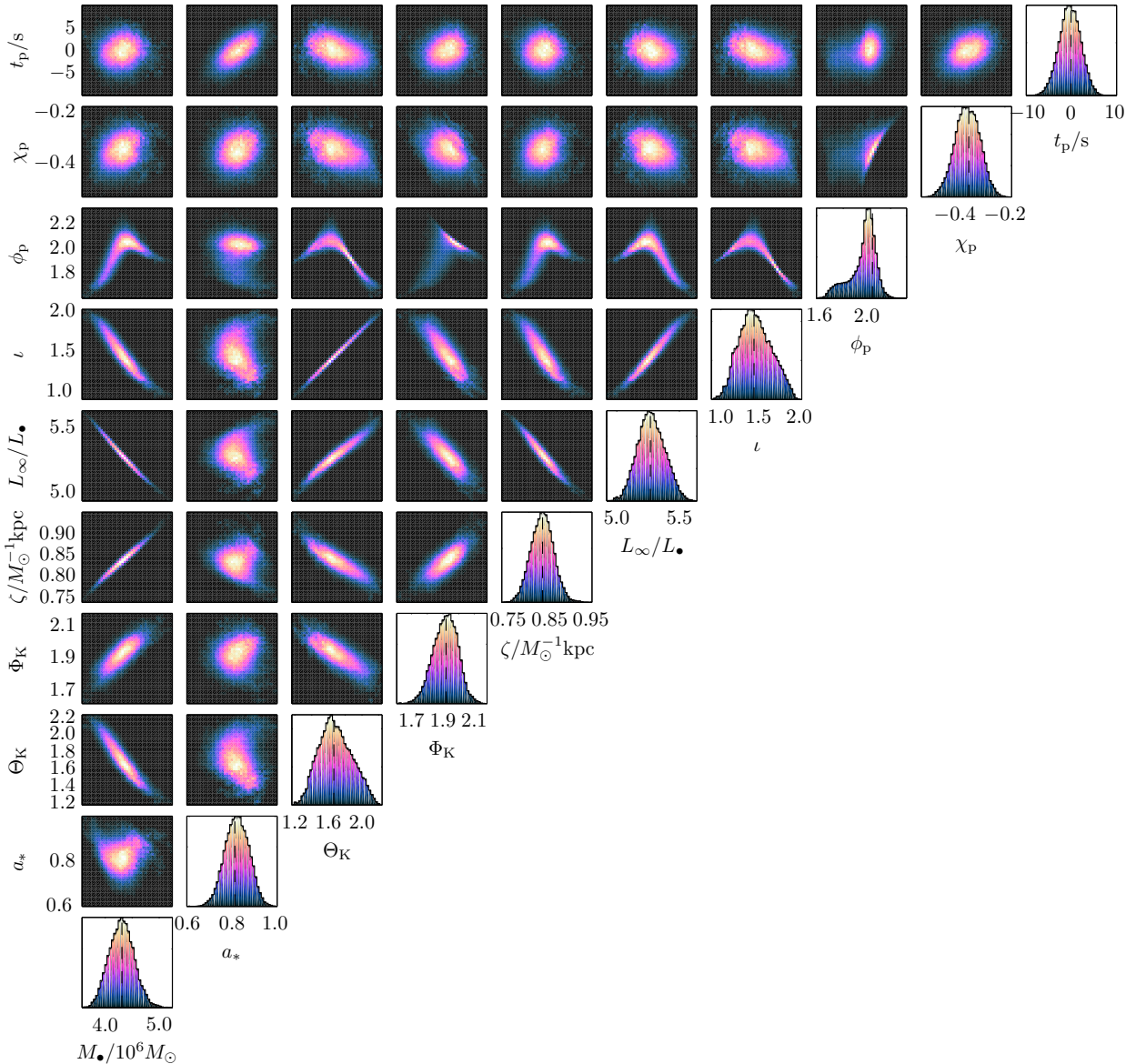


Figure 11. Marginalised one and two dimensional posteriors. The scales are identical in both sets of plots. The dotted line indicates the true value. These distributions show complicated degeneracies. The input orbit has $r_p \simeq 11.60r_g$ and $\rho \simeq 590$.

best agreement is for t_p , which is largely uncorrelated with the other parameters. The widths for M_\bullet , a_* , L_∞ and ι show more severe differences; these parameters show the tightest degeneracies. The two methods do show signs of slowly converging with increasing SNR, as expected.

As a consistency check, to verify that the mismatch between the FIM and MCMC results is a consequence of parameter correlations, we calculated one-dimensional FIMs, only varying the MBH mass, and compared these to widths computed from MCMCs only sampling in mass. These were found to be in good agreement. The majority ($\sim 87\%$) have standard deviations consistent to within a factor of two; the rest within an order of magnitude.¹⁴ Some small difference is

expected because of numerical error from calculating derivatives for the FIM by finite differencing.

8.3 Scientific potential

Having quantified the precision with which we could infer parameters from an EMRB waveform, we can now consider if it is possible to learn anything new.

Of paramount interest are the MBH mass and spin. The current uncertainty in the mass is $\sigma_{M_\bullet} = 0.36 \times 10^6 M_\odot$ ($\sim 8\%$). There are few runs amongst our data set that are not better than this: it appears that orbits of a $\mu = 10 M_\odot$ CO with periapses $r_p \lesssim 13r_g$ should be able to match our

¹⁴ One differed by more than an order of magnitude, and also

failed to fulfil the (one dimensional) MM criterion; this was a numerical problem in calculating the FIM.

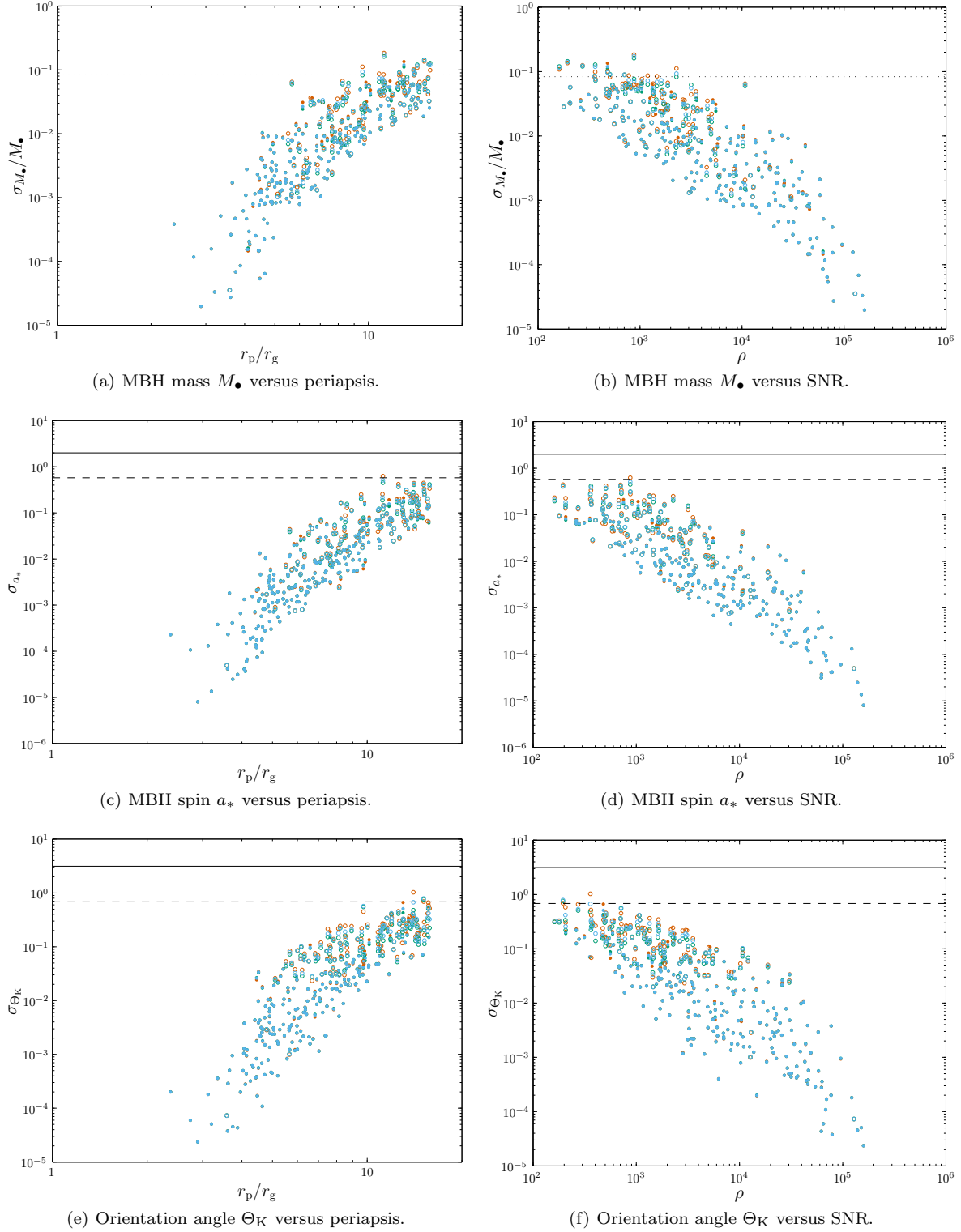


Figure 12. Distribution widths as functions of periaxis r_p and SNR ρ . Light blue is used for the standard deviation, red is the scaled 50-percentile range and green is the scaled 95-percentile range: all three coincide for a normal distribution. Filled circles are used for converged runs, open circles for those yet to converge. The dotted line indicates the current uncertainty for M_\bullet ; the dashed lines the standard deviation for an uninformative prior, and the solid lines the total prior range.

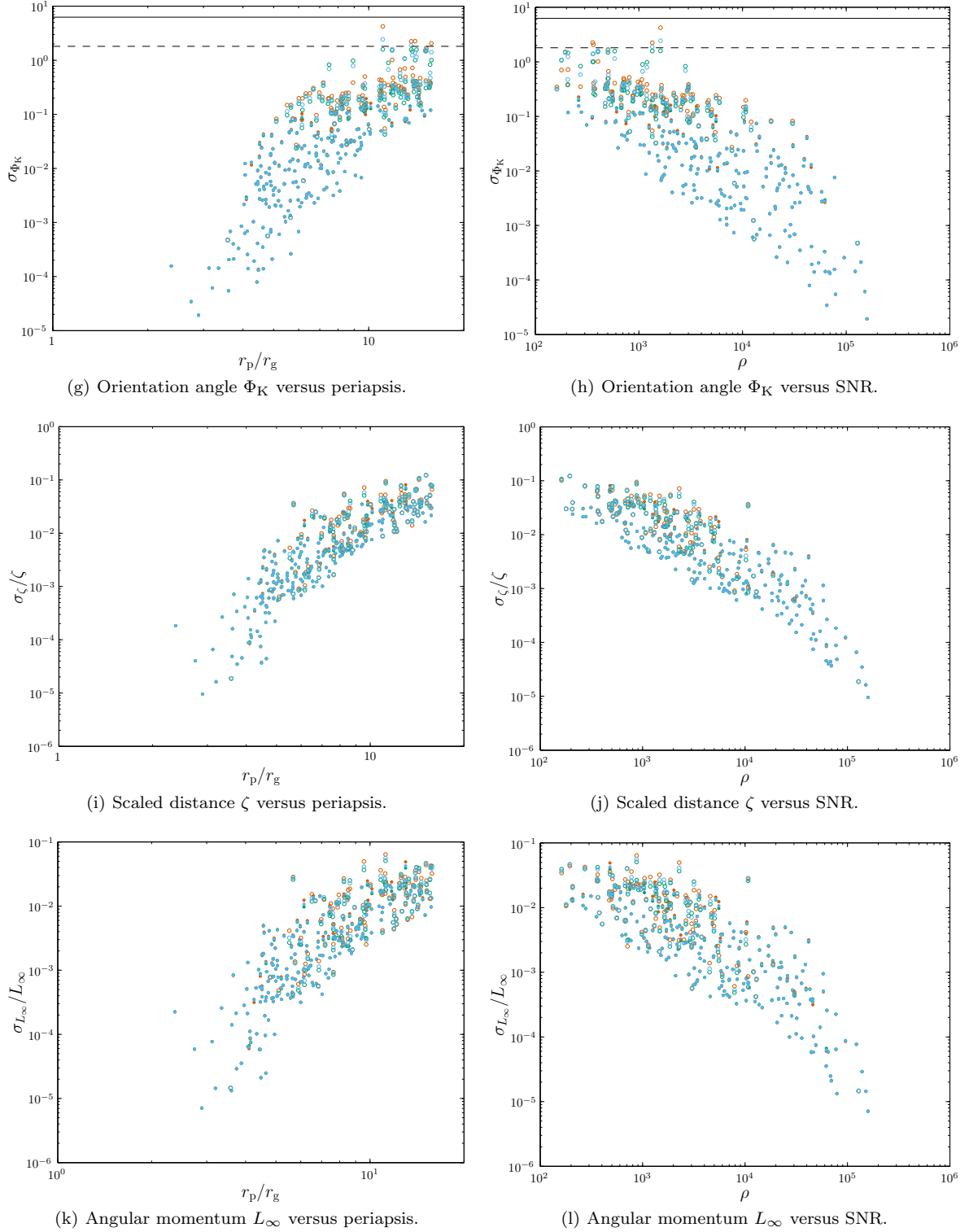


Figure 12 – continued Distribution widths as functions of periape r_p and SNR ρ . Light blue is used for the standard deviation, red is the scaled 50-percentile range and green is the scaled 95-percentile range: all three coincide for a normal distribution. Filled circles are used for converged runs, open circles for those yet to converge. The dotted line indicates the current uncertainty for M_\bullet ; the dashed lines the standard deviation for an uninformative prior, and the solid lines the total prior range.

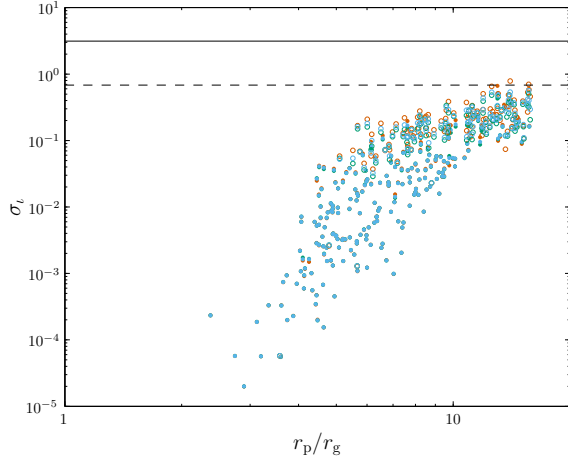
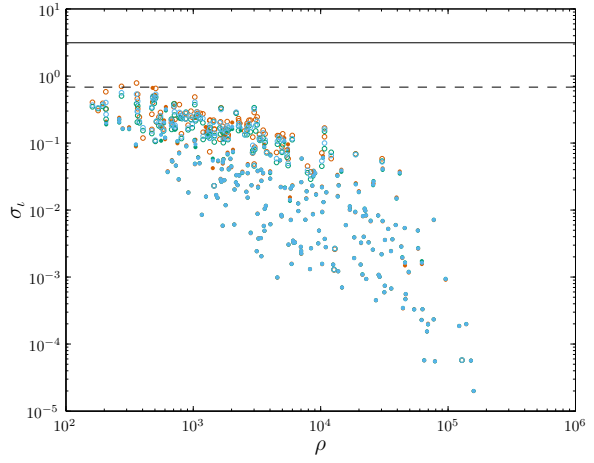
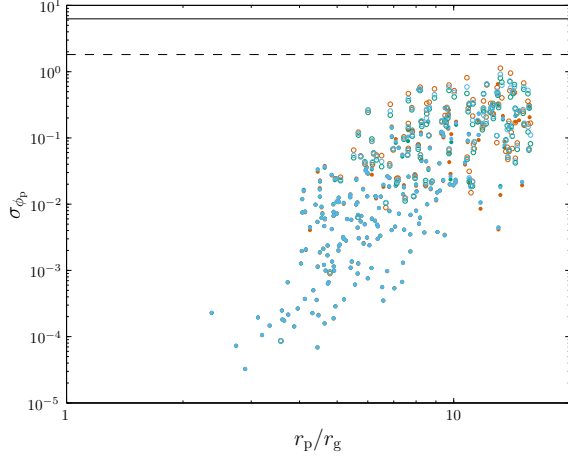
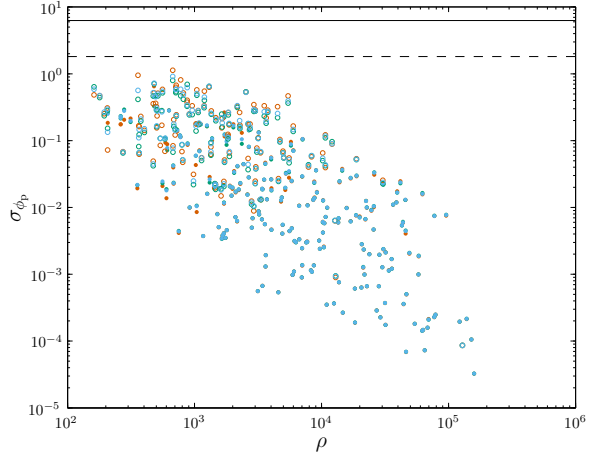
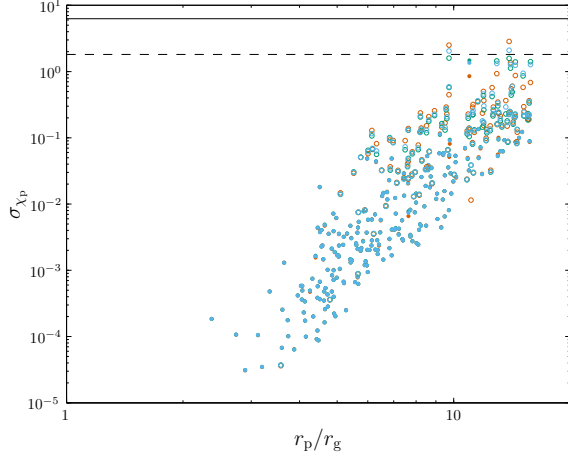
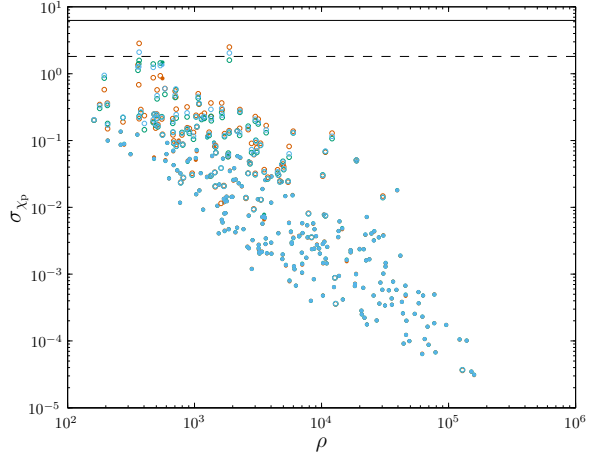
(m) Orbital inclination i versus periapsis.(n) Orbital inclination i versus SNR.(o) Periapse azimuthal phase ϕ_p versus periapsis.(p) Periapse azimuthal phase ϕ_p versus SNR.(q) Periapse polar phase χ_p versus periapsis.(r) Periapse polar phase χ_p versus SNR.

Figure 12 – continued Distribution widths as functions of periapse r_p and SNR ρ . Light blue is used for the standard deviation, red is the scaled 50-percentile range and green is the scaled 95-percentile range: all three coincide for a normal distribution. Filled circles are used for converged runs, open circles for those yet to converge. The dotted line indicates the current uncertainty for M_\bullet ; the dashed lines the standard deviation for an uninformative prior, and the solid lines the total prior range.

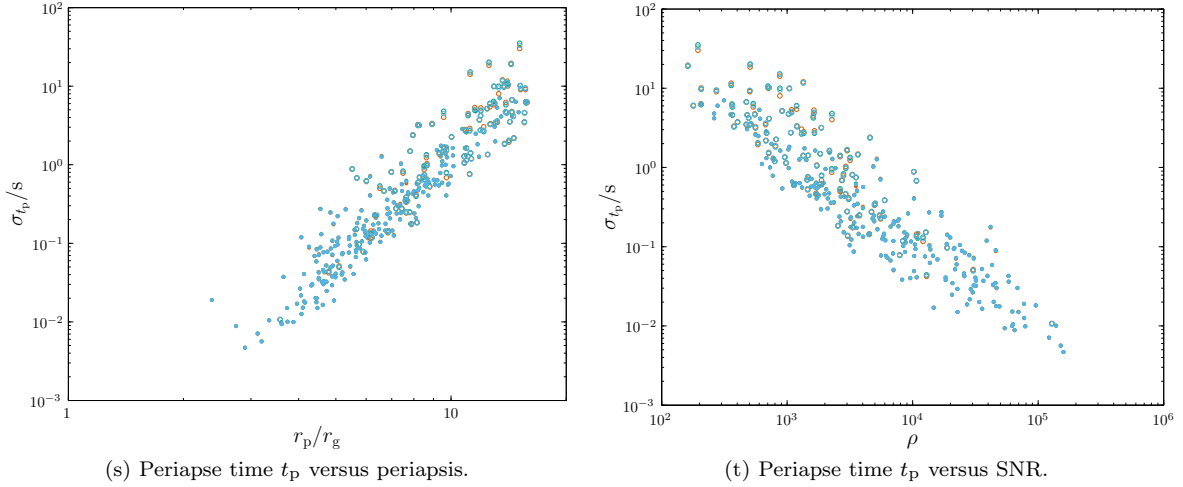


Figure 12 – continued Distribution widths as functions of periapsis r_p and SNR ρ . Light blue is used for the standard deviation, red is the scaled 50-percentile range and green is the scaled 95-percentile range: all three coincide for a normal distribution. Filled circles are used for converged runs, open circles for those yet to converge. The dotted line indicates the current uncertainty for M_\bullet ; the dashed lines the standard deviation for an uninformative prior, and the solid line the total prior range.

current observational constraints. However, the EMRB is an independent measurement, and so a measurement of comparable precision to the current bound can still be informative. Accuracy of 1% could be possible if $r_p \lesssim 8r_g$.

The spin is less well constrained. To obtain an uncertainty for the magnitude of 0.1, comparable to that achieved in X-ray measurements of active galactic nuclei, it appears that the periapsis needs to be $r_p \lesssim 11r_g$. For smaller periapses, the uncertainty can be much less, indicating that an EMRB could be an excellent probe. The orientation angles for the spin axis may be constrained to better than 0.1 for $r_p \lesssim 11r_g$. It may well be possible to learn both the direction and the magnitude of the spin. This could illuminate the MBH's formation.

We have no *a priori* knowledge about the CO or its orbit, so anything we learn would be new. However, this is not particularly useful information, unless we observe multiple bursts, and can start to build up statistics for the dynamics of the GC. Using current observations for the distance to the GC, which could be further improved by the mass measurement from the EMRB, it is possible to infer a value for the mass μ from ζ . This could inform us of the nature of the object (BH, NS or WD) and be a useful consistency check. A small value of ζ , indicating a massive CO, would be unambiguous evidence for the existence of a stellar mass BH.

9 EXTRA-GALACTIC SOURCES

We have so far only been concerned with properties of bursts from our own galaxy. This is the best source for bursts because of its proximity. A natural continuation is to consider EMRBs from other MBHs. Rubbo et al. (2006) suggested that *LISA* should be able to detect EMRBs originating from the Virgo cluster, although the detectable rate may be only 10^{-4} yr $^{-1}$ per galaxy (Hopman et al. 2007). Detectability depends upon the mass of the MBH; higher masses correspond to lower frequency bursts, which are harder to detect.

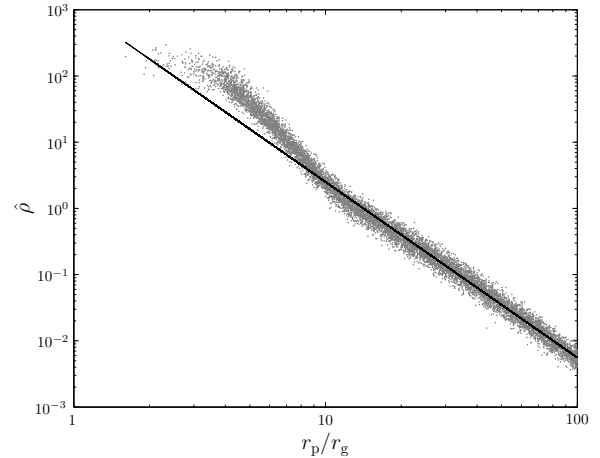


Figure 14. Signal-to-noise ratio as a function of periapse radius for a $\mu = 1M_\odot$ CO about the MBH of M32. The plotted points are the values obtained by averaging over each set of intrinsic parameters. The best fit line is $\log(\rho) = -2.65 \log(r_p/r_g) + 3.05$. This is fitted to orbits with $r_p > 18.8r_g$ and has a reduced chi-squared value of $\chi^2/\nu = 1.26$.

Checking our nearest neighbours, we find bursts from Andromeda (M31) would not be detectable. This is because of the large mass of the MBH $M_{\text{M31}} = (1.4^{+0.9}_{-0.3}) \times 10^8 M_\odot$ (Bender et al. 2005). However, its companion M32 is more promising. It has a lighter MBH $M_{\text{M32}} = (2.5 \pm 0.5) \times 10^6 M_\odot$ (Verolme et al. 2002). The trend between the periapse radius and SNR is shown in Fig. 14. The fit is again for orbits with $f_* = \sqrt{GM_{\text{M32}}/r_p} < 1 \times 10^{-3}$ Hz to avoid the bucket of the noise curve. Bursts for a $1M_\odot$ ($10M_\odot$) can be detected with $\rho > 10$ if the periapse is smaller than $7r_g$ ($14r_g$).

The general behaviour is the same as for the GC. Bursts from the two MBHs can be compared using their characteristic frequencies f_* and scaled SNR

$$\rho_*[\mathbf{h}] = \left(\frac{\mu}{M_\odot} \right)^{-1} \left(\frac{R}{\text{kpc}} \right) \left(\frac{M}{10^6 M_\odot} \right)^{-2/3} \rho[\mathbf{h}], \quad (42)$$

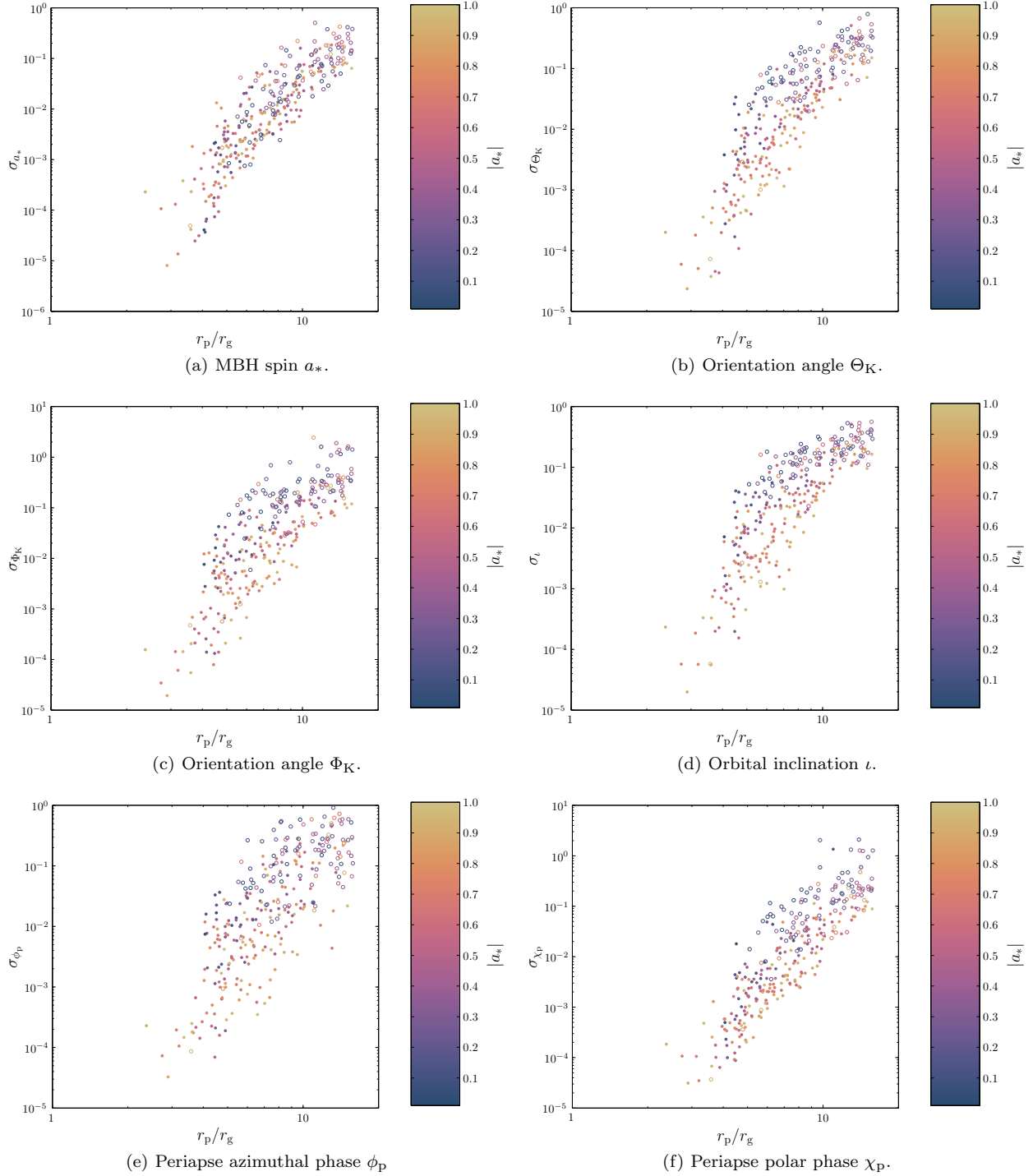


Figure 13. Parameter standard deviations versus periapsis r_p , showing dependence (or lack thereof) upon the spin magnitude $|a_*$.

where R and M are the appropriate distances and masses for the two MBHs. These scalings can be determined from the quadrupole piece of (14) assuming a characteristic length scale set by r_p . Figure 15 shows the trend for both galaxies. The difference in sky position is largely washed out through the motion of the detector.

M31 and M32 are at a distance of 770 kpc (Karachentsev et al. 2004). It therefore seems unlikely that

bursts could be observed from the Virgo cluster at a distance of $R_{\text{Virgo}} \approx 16.5$ Mpc (Mei et al. 2007).

Triangulum (M33) is believed not to have an MBH. Merritt et al. (2001) use dynamical constraints to place an upper bound on the mass of a central BH of $M_{\text{M33}} < 3 \times 10^3 M_\odot$, Gebhardt et al. (2001) find a bound of $M_{\text{M33}} < 1.5 \times 10^3 M_\odot$. Observations of the ultra-luminous nuclear X-ray source (ULX) closest to the centre of M33 yield a best estimate of $M_{\text{ULX}} \sim \mathcal{O}(10) M_\odot$ for the source object's mass

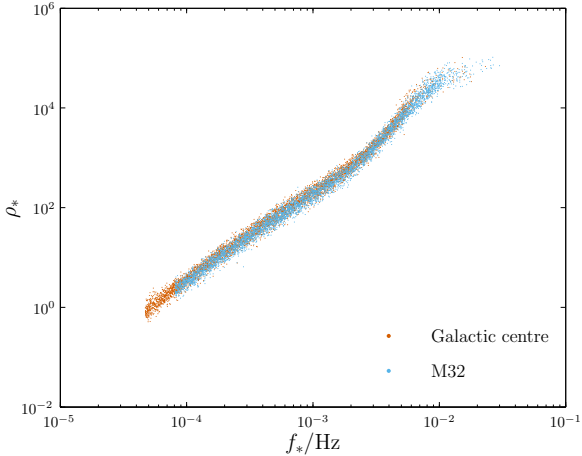


Figure 15. Scaled signal-to-noise ratio as a function of characteristic frequency.

(Foschini et al. 2004; Weng et al. 2009). This is consistent with there being no MBH; the ULX originates from a stellar mass BH that is coincidentally located close to the core of the galaxy. Consequently, we do not expect to see any bursts from M33: to detect one would confirm the existence of a previously invisible MBH.

10 DISCUSSION

We have outlined an approximate method of generating gravitational waveforms for EMRBs originating at the GC. This assumes that the orbits are parabolic and employs a numerical kludge approximation. The two coordinate schemes for a NK presented here yield almost indistinguishable results. We conclude that either is a valid choice for this purpose. There may be differences when the spin is large and the periapse is small: $\sim 10\%$ for $r_p \simeq 4r_g$, $\sim 20\%$ for $r_p \simeq 2r_g$.

The waveforms created appear to be consistent with results obtained using Peters and Mathews waveforms for large periapses, indicating that they have the correct weak-field form. The NK approach should be superior to that of Peters and Mathews in the strong-field regime as it uses the exact geodesics of the Kerr spacetime. Comparisons with energy fluxes from black hole perturbation theory indicate that typical waveform accuracy may be of order 5%, but this is worse for orbits with small periapses and may be $\sim 20\%$. These errors are greater than the differences resulting from the use of the alternative coordinate systems.

The signal-to-noise ratio of bursts is well correlated with the periapsis. Except for the closest orbits ($r_p \lesssim 7r_g$), the SNR (per unit mass) may be reasonably described as having a power-law dependence of

$$\log(\hat{\rho}) \simeq -2.7 \log\left(\frac{r_p}{r_g}\right) + 4.9. \quad (43)$$

Signals should be detectable for a $1M_\odot$ ($10M_\odot$) object if the periapse is $r_p < 27r_g$ ($r_p < 65r_g$), corresponding to a physical scale of 1.7×10^{11} m (4.1×10^{11} m) or 5.6×10^{-6} pc (1.3×10^{-5} pc).

Using the NK waveforms we conducted an investigation, using Fisher matrix analysis, into how precisely we could

infer parameters of the GC's MBH should such an EMRB be observed. However, we found that the linearised-signal approximation does not hold for these bursts over a wide range of SNR. This demonstrates the necessity of checking the approximation before quoting the results of an analysis (Vallisneri 2008).

We used MCMC results as a more robust measure of parameter estimation accuracy. Potentially, it is possible to determine very precisely the key parameters defining the MBH's mass and spin, if the orbit gets close enough to the MBH. It appears that we can achieve good results from a single EMRB with periapsis of $r_p \simeq 10r_g$ for a $10M_\odot$ CO. This translates to a distance of 6×10^{10} m or 2×10^{-6} pc. Orbits closer than this would place stricter constraints. The best orbits yield uncertainties of almost one part in 10^5 for the MBH mass and spin, far exceeding existing techniques. Conversely, orbits with $r_p \gtrsim 20r_g$ are unlikely to provide any useful information.

Before we can quote results for how accurately we can determine the various parameters, we must consider the probability of each orbit. This will be the subject of a companion paper, building upon the earlier results of Rubbo et al. (2006) and Hopman et al. (2007), who only considered approximate forms for the SNR, rather than using waveforms. Using a model for the nuclear star cluster of the GC it is possible to define distributions for angular momenta L_∞ , for a species of mass μ . With these we can estimate the event rate and how much information, on average, we could hope to obtain from EMRB observations. If it is likely that we would observe multiple EMRBs, it may be possible to combine results to tighten uncertainties.

Some consideration should also be given to methods of fitting a waveform to an observed signal. Given a noisy data stream, how could EMRBs be extracted? The parabolic spectrum has a characteristic profile, suggesting that matched filtering could be possible. Complications could arise in fitting parameters to a waveform: we have seen that there exist complicated degeneracies between parameters. These issues would warrant further investigation should the event rate be high enough.

While we have only considered bursts from our own galaxy in detail, it should be possible to observe bursts from other nearby galaxies if their MBH is of the appropriate mass. This makes M32 a viable candidate. The SNR shows a similar dependence upon periapsis as for the GC, and may be described by a power-law of

$$\log(\hat{\rho}) \simeq -2.7 \log\left(\frac{r_p}{r_g}\right) + 3.1, \quad (44)$$

for orbits with $r_p \gtrsim 10r_g$. For a $1M_\odot$ ($10M_\odot$) object, bursts should be detectable for periapses $r_p \lesssim 7r_g$ ($r_p \lesssim 14r_g$), corresponding to 2.6×10^{10} m (4.9×10^{10} m) or 8.4×10^{-7} pc (1.6×10^{-6} pc). This is a small region of parameter space, so we conclude that extra-galactic bursts are likely to be rare.

ACKNOWLEDGMENTS

The authors are indebted to Michele Vallisneri for discussions on the (im)proper use of Fisher matrices; they thank Stephen Taylor for advice on adaptive MCMC methods and Dave Green for helpful suggestions regarding apodization.

They are grateful to Donald Lynden-Bell for his suggestions, and would like to thank Pau Amaro-Seoane for useful comments. CPLB is supported by STFC. JRG is supported by the Royal Society. The MCMC simulations were performed using the Darwin Supercomputer of the University of Cambridge High Performance Computing Service (<http://www.hpc.cam.ac.uk/>), provided by Dell Inc. using Strategic Research Infrastructure Funding from the Higher Education Funding Council for England. Figures 9, 10 and 11 were produced using the colour scheme of Green (2011).

REFERENCES

- Alexander T., Hopman C., 2009, ApJ, 697, 1861
 Amaro-Seoane P., 2012, Stellar dynamics and extreme-mass ratio inspirals, arXiv:1205.5240 [astro-ph.CO]
 Amaro-Seoane P. et al., 2012a, Classical Quant. Grav., 29, 124016
 Amaro-Seoane P. et al., 2012b, eLISA: Astrophysics and cosmology in the millihertz regime, arXiv:1201.3621 [astro-ph.CO]
 Amaro-Seoane P., Gair J. R., Freitag M., Miller M. C., Mandel I., Cutler C. J., Babak S., 2007, Classical Quant. Grav., 24, R113
 Amaro-Seoane P., Pretorius F., 2011, Classical and Quant. Grav., 28, 094017
 Andrieu C., Thoms J., 2008, Statistics and Computing, 18, 343
 Babak S., Fang H., Gair J., Glampedakis K., Hughes S., 2007, Phys. Rev. D, 75, 024005
 Backer D. C., Sramek R. A., 1999, ApJ, 524, 805
 Bahcall J. N., Wolf R. A., 1977, ApJ, 216, 883
 Barack L., 2009, Classical Quant. Grav., 26, 213001
 Barack L., Cutler C., 2004, Phys. Rev. D, 69, 082005
 Bédard M., 2007, The Annals of Applied Probability, 17, 1222
 Bédard M., 2008a, Journal of Computational and Graphical Statistics, 17, 312
 Bédard M., 2008b, Stochastic Processes and their Applications, 118, 2198
 Bekenstein J. D., 1973, ApJ, 183, 657
 Bender P. et al., 1998, LISA Pre-Phase A Report. Tech. rep., Max-Planck-Institut für Quantenoptik, Garching
 Bender R. et al., 2005, ApJ, 631, 280
 Berry C. P. L., Gair J. R., 2010, Phys. Rev. D, 82, 107501
 Berti E., Cardoso V., Gonzalez J. A., Sperhake U., Hannam M., Husa S., Brügmann B., 2007, Phys. Rev. D, 76, 064034
 Berti E., Volonteri M., 2008, ApJ, 684, 822
 Boyer R. H., Lindquist R. W., 1967, Journal of Mathematical Physics, 8, 265
 Brenneman L. W., Reynolds C. S., 2006, ApJ, 652, 1028
 Burko L. M., Khanna G., 2007, EPL, 78, 60005
 Carter B., 1968, Phys. Rev., 174, 1559
 Chabrier G., Baraffe I., 2000, ARA&A, 38, 337
 Chandrasekhar S., 1998, The Mathematical Theory of Black Holes, Oxford Classic Texts in the Physical Sciences. Oxford University Press, Oxford
 Cutler C., 1998, Phys. Rev. D, 57, 7089
 Cutler C., Flanagan E. E., 1994, Phys. Rev. D, 49, 2658
 Damour T., Iyer B. R., Sathyaprakash B. S., 2000, Phys. Rev. D, 62, 084036
 Danzmann K., Rüdiger A., 2003, Classical Quant. Grav., 20, S1
 de Felice F., 1980, Journal of Physics A, 13, 1701
 de la Calle Pérez I. et al., 2010, A&A, 524, A50
 Doeleman S. S. et al., 2008, Nat, 455, 78
 Drasco S., Hughes S., 2004, Phys. Rev. D, 69, 044015
 Finn L. S., 1992, Phys. Rev. D, 46, 5236
 Foschini L., Rodriguez J., Fuchs Y., Ho L. C., Dadina M., Di Cocco G., Courvoisier T. J.-L., Malagutti G., 2004, Astronomy and Astrophysics, 416, 529
 Freitag M., 2003, ApJ, 583, L21
 Gair J. R., Kennefick D. J., Larson S. L., 2005, Phys. Rev. D, 72, 084009
 Gammie C. F., Shapiro S. L., McKinney J. C., 2004, ApJ, 602, 312
 Gebhardt K. et al., 2001, AJ, 122, 2469
 Gelman A., Roberts G. O., Gilks W. R., 1996, in Bayesian Statistics, Bernardo J. M., Berger J. O., Dawid A. P., Smith A. F. M., eds., Valencia International Meeting, Oxford University Press, Oxford, pp. 599–607
 Genzel R., Schödel R., Ott T., Eckart A., Alexander T., Lacombe F., Rouan D., Aschenbach B., 2003, Nat, 425, 934
 Ghez A. M. et al., 2008, ApJ, 689, 1044
 Gillessen S., Eisenhauer F., Trippe S., Alexander T., Genzel R., Martins F., Ott T., 2009, ApJ, 692, 1075
 Glampedakis K., 2005, Classical Quant. Grav., 22, S605
 Glampedakis K., Hughes S., Kennefick D., 2002, Phys. Rev. D, 66, 064005
 Glampedakis K., Kennefick D., 2002, Phys. Rev. D, 66, 044002
 González J. A., Sperhake U., Brügmann B., Hannam M., Husa S., 2007, Phys. Rev. Lett., 98, 091101
 Graham A. W., Erwin P., Caon N., Trujillo I., 2001, ApJ, 563, L11
 Graham A. W., Onken C. A., Athanassoula E., Combes F., 2011, MNRAS, 412, 2211
 Green D. A., 2011, Bulletin of the Astronomical Society of India, 39, 289
 Haario H., Saksman E., Tamminen J., 1999, Computational Statistics, 14, 375
 Haario H., Saksman E., Tamminen J., 2001, Bernoulli, 7, 223
 Haiman Z., Quataert E., 2004, The Formation and Evolution of the First Massive Black Holes, Barger A. J., ed., Astrophysics and Space Science Library, Kluwer Academic Publishers, Dordrecht, pp. 147–186
 Hamalainen N., Paumard T., Müller T., Gillessen S., Eisenhauer F., Trippe S., Genzel R., 2009, ApJ, 692, 902
 Harris F., 1978, Proceedings of the IEEE, 66, 51
 Hastings W. K., 1970, Biometrika, 57, 97
 Hobson M. P., Efstathiou G., Lasenby A., 2006, General Relativity: An Introduction for Physicists. Cambridge University Press, Cambridge
 Hopman C., Freitag M., Larson S. L., 2007, MNRAS, 378, 129
 Huerta E. A., Gair J. R., 2009, Phys. Rev. D, 79, 84021
 Hughes S. A., Blandford R. D., 2003, ApJ, 585, L101
 Jahnke K., Macciò A. V., 2011, ApJ, 734, 92
 Jaynes E. T., 2003, Probability Theory: The Logic of Science. Cambridge University Press, Cambridge
 Jennrich O. et al., 2011, NGO Revealing a hidden Universe:

- opening a new chapter of discovery. Tech. rep., European Space Agency
- Kaiser J., Schafer R., 1980, IEEE Trans. Acoustics, Speech and Signal Processing, 28, 105
- Karachentsev I. D., Karachentseva V. E., Huchtmeier W. K., Makarov D. I., 2004, AJ, 127, 2031
- Kato Y., Miyoshi M., Takahashi R., Negoro H., Matsumoto R., 2010, MNRAS, 403, L74
- Kerr R., 1963, Phys. Rev. Lett., 11, 237
- King A. R., Pringle J. E., 2006, MNRAS, 373, L90
- King A. R., Pringle J. E., Hofmann J. A., 2008, MNRAS, 385, 1621
- Kormendy J., Richstone D., 1995, ARA&A, 33, 581
- Lynden-Bell D., Rees M. J., 1971, MNRAS, 152, 461
- MacKay D. J. C., 2003, Information Theory, Inference and Learning Algorithms. Cambridge University Press, Cambridge, p. 640
- Magorrian J. et al., 1998, AJ, 115, 2285
- Malbon R. K., Baugh C. M., Frenk C. S., Lacey C. G., 2007, MNRAS, 382, 1394
- Martel K., 2004, Phys. Rev. D, 69, 044025
- McClintock J. E. et al., 2011, Classical Quant. Grav., 28, 114009
- McKeehan D. J. A., Robinson C., Sathyaprakash B. S., 2010, Classical Quant. Grav., 27, 084020
- Mei S. et al., 2007, ApJ, 655, 144
- Merritt D., Alexander T., Mikkola S., Will C. M., 2010, Phys. Rev. D, 81, 062002
- Merritt D., Ferrarese L., Joseph C. L., 2001, Sci, 293, 1116
- Metropolis N., Rosenbluth A. W., Rosenbluth M. N., Teller A. H., Teller E., 1953, The Journal of Chemical Physics, 21, 1087
- Miller J., 2007, ARA&A, 45, 441
- Miniutti G., Panessa F., De Rosa A., Fabian A. C., Malizia A., Molina M., Miller J. M., Vaughan S., 2009, MNRAS, 398, 255
- Misner C. W., Thorne K. S., Wheeler J. A., 1973, Gravitation. W. H. Freeman, New York
- Nardini E., Fabian A. C., Reis R. C., Walton D. J., 2011, MNRAS, 410, 1251
- Nuttall A., 1981, IEEE Transactions on Acoustics, Speech and Signal Processing, 29, 84
- Patrick A. R., Reeves J. N., Porquet D., Markowitz A. G., Lobban A. P., Terashima Y., 2011, MNRAS, 411, 2353
- Peng C. Y., 2007, ApJ, 671, 1098
- Peters P. C., 1964, Phys. Rev., 136, B1224
- Peters P. C., Mathews J., 1963, Phys. Rev., 131, 435
- Press W., 1977, Phys. Rev. D, 15, 965
- Preto M., Amaro-Seoane P., 2010, ApJ, 708, L42
- Psaltis D., 2008, Living Reviews in Relativity, 11
- Rees M. J., 1984, ARA&A, 22, 471
- Reid M. J., Menten K. M., Genzel R., Ott T., Schödel R., Brunthaler A., 2003, Astronomische Nachrichten, 324, 505
- Reid M. J., Readhead A. C. S., Vermeulen R. C., Treuhaft R. N., 1999, ApJ, 524, 816
- Roberts G. O., Gelman A., Gilks W. R., 1997, The Annals of Applied Probability, 7, 110
- Roberts G. O., Rosenthal J. S., 2001, Statistical Science, 16, 351
- Roberts G. O., Rosenthal J. S., 2007, Journal of Applied Probability, 44, 458
- Rosquist K., Bylund T., Samuelsson L., 2009, International Journal of Modern Physics D, 18, 429
- Rubbo L. J., Holley-Bockelmann K., Finn L. S., 2006, ApJ, 649, L25
- Ruffini R., Sasaki M., 1981, Progress of Theoretical Physics, 66, 1627
- Sathyaprakash B., Schutz B. F., 2009, Living Reviews in Relativity, 12
- Schmoll S. et al., 2009, ApJ, 703, 2171
- Sikora M., Stawarz L., Lasota J.-P., 2007, ApJ, 658, 815
- Tanaka T., Shibata M., Sasaki M., Tagoshi H., Nakamura T., 1993, Progress of Theoretical Physics, 90, 65
- Thorne K. S., 1974, ApJ, 191, 507
- Tremaine S. et al., 2002, ApJ, 574, 740
- Turner M., 1977, ApJ, 216, 610
- Vallisneri M., 2008, Phys. Rev. D, 77, 042001
- Verolme E. K. et al., 2002, MNRAS, 335, 517
- Volonteri M., 2010, A&AR, 18, 279
- Volonteri M., Madau P., Quataert E., Rees M. J., 2005, ApJ, 620, 69
- Volonteri M., Natarajan P., 2009, MNRAS, 400, 1911
- Volonteri M., Sikora M., Lasota J.-P., 2007, ApJ, 667, 704
- Weng S.-S., Wang J.-X., Gu W.-M., Lu J.-F., 2009, PASJ, 61, 1287
- Wilkins D., 1972, Phys. Rev. D, 5, 814
- Yu Q., Tremaine S., 2002, MNRAS, 335, 965
- Yunes N., Sopuerta C. F., Rubbo L. J., Holley-Bockelmann K., 2008, ApJ, 675, 604
- Yusef-Zadeh F., Choate D., Cotton W., 1999, ApJ, 518, L33
- Zoghbi A., Fabian A. C., Uttley P., Miniutti G., Gallo L. C., Reynolds C. S., Miller J. M., Ponti G., 2010, MNRAS, 401, 2419

APPENDIX A: WINDOW FUNCTIONS

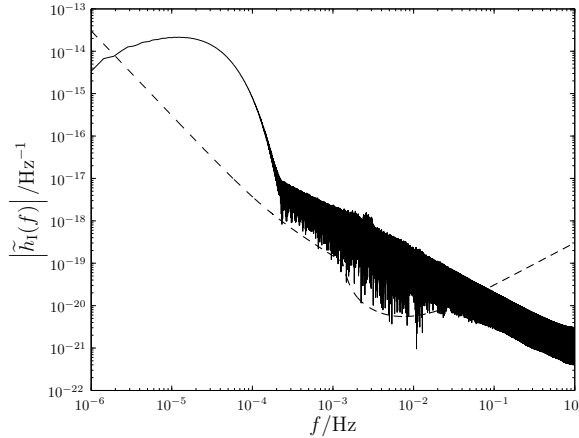
When performing a Fourier transform using a computer we must necessarily only transform a finite time-span τ . The effect of this is the same as transforming the true, infinite signal multiplied by a unit top-hat function of width τ . Transforming yields the true waveform convolved with a sinc. If $\tilde{h}'(f)$ is the computed Fourier transform then

$$\tilde{h}'(f) = \int_{-\tau/2}^{\tau/2} h(t) \exp(2\pi ift) dt = [\tilde{h}(f) * \tau \operatorname{sinc}(\pi f \tau)], \quad (\text{A1})$$

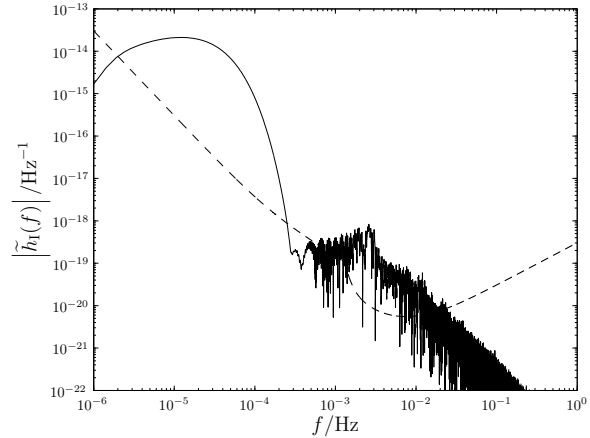
where $\tilde{h}(f) = \mathcal{F}\{h(t)\}$ is the unwindowed Fourier transform of the infinite signal. This windowing of the data is a problem innate in the method, and results in spectral leakage.

Fig. A1(a) shows the computed Fourier transform for an example EMRB. The waveform has two distinct regions: a low-frequency curve, and a high-frequency tail. The low-frequency signal is the spectrum we are interested in; the high-frequency components are a combination of spectral leakage and numerical noise. The $\mathcal{O}(1/f)$ behaviour of the sinc gives the shape of the tail. This has possibly been misidentified in figure 8 of Burko & Khanna (2007) as the characteristic strain for parabolic encounters.

Despite being many orders of magnitude below the peak level, the high-frequency tail is still well above the noise curve for a wide range of frequencies. It therefore contributes



(a) Spectrum using no window. The calculated SNR is $\rho \simeq 12.5$.



(b) Spectrum using a Nuttall window. The calculated SNR is $\rho \simeq 8.5$.

Figure A1. Example spectra calculated using (a) a rectangular window and (b) Nuttall's four-term window with continuous first derivative (Nuttall 1981). The spin of the MBH is $a_* = 0.5$, the mass of the orbiting CO is $\mu = 10M_\odot$, the periapsis is $r_p = 50r_g$ and the inclination is $i = 0.1$. The high-frequency tail is the result of spectral leakage. The level of the LISA noise curve is indicated by the dashed line. The spectra are from detector I, but the detector II spectra look similar.

to the evaluation of any inner products, and could mask interesting features. It is possible to reduce the leakage using apodization: to improve the frequency response of a finite time series one can use a weighting window function $w(t)$ which modifies the impulse response in a prescribed way.

The simplest window function is the rectangular (or Dirichlet) window $w_R(t)$; this is the top-hat described above. Other window functions are generally tapered.¹⁵ There is a wide range of window functions described in the literature (Harris 1978; Kaiser & Schafer 1980; Nuttall 1981; McKeehan, Robinson, & Sathyaprakash 2010). The introduction of a window function influences the spectrum in a manner dependent upon its precise shape. There are two distinct distortions: local smearing due to the finite width of the centre lobe, and distant leakage due to finite amplitude sidelobes. The window function may be optimised such that the peak sidelobe has a small amplitude, or such that the sidelobes decay away rapidly with frequency. Choosing a window function is a trade-off between these various properties, and depends upon the particular application.

For use with the parabolic spectra, the primary concern is to suppress the sidelobes. Many windows with good side-lobe behaviour exist; we consider three: the Blackman-Harris minimum four-term window (Harris 1978; Nuttall 1981)

$$w_{BH}(t) = \sum_{n=0}^3 a_n^{BH} \cos\left(\frac{2n\pi t}{\tau}\right), \quad (\text{A2})$$

where

$$\begin{aligned} a_0^{BH} &= 0.35875, & a_1^{BH} &= 0.48829, \\ a_2^{BH} &= 0.14128, & a_3^{BH} &= 0.01168; \end{aligned} \quad (\text{A3})$$

the Nuttall four-term window with continuous first derivative (Nuttall 1981)

¹⁵ When using a tapered window function it is important to ensure that the window is centred upon the signal; otherwise the calculated transform has a reduced amplitude.

and the Kaiser-Bessel window (Harris 1978; Kaiser & Schafer 1980)

$$w_{KB}(t; \beta) = \frac{I_0[\beta\sqrt{1-(2t/\tau)^2}]}{I_0(\beta)}, \quad (\text{A6})$$

where $I_\nu(z)$ is the modified Bessel function of the first kind, and β is an adjustable parameter. Increasing β reduces the peak sidelobe, but also widens the central lobe.

The Kaiser-Bessel window has the smallest peak sidelobe, but the worst decay ($1/f$); the Nuttall window has the best asymptotic behaviour ($1/f^3$); the Blackman-Harris window has a peak sidelobe similar to the Nuttall window, and decays asymptotically as fast (slow) as the Kaiser-Bessel window, but has the advantage of having suppressed sidelobes next to the central lobe.

Another window has been recently suggested for use with gravitational waveforms: the Planck-taper window (Damour, Iyer, & Sathyaprakash 2000; McKeehan et al. 2010)

$$w_P(t; \epsilon) = \begin{cases} \frac{1}{\exp(Z_+) + 1} & -\frac{\tau}{2} \leq t < -\tau\left(\frac{1}{2} - \epsilon\right) \\ 1 & -\tau\left(\frac{1}{2} - \epsilon\right) < t < \tau\left(\frac{1}{2} - \epsilon\right) \\ \frac{1}{\exp(Z_-) + 1} & -\tau\left(\frac{1}{2} - \epsilon\right) < t \leq \frac{\tau}{2} \end{cases}, \quad (\text{A7})$$

with

$$Z_\pm(t; \epsilon) = 2\epsilon \left[\frac{1}{1 \pm 2(t/\tau)} + \frac{1}{1 - 2\epsilon \pm 2(t/\tau)} \right]. \quad (\text{A8})$$

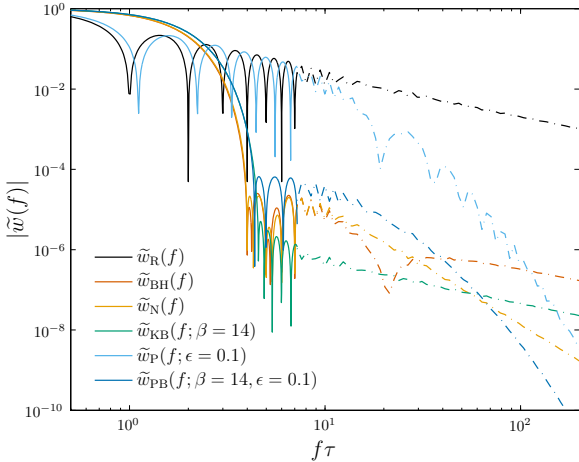


Figure A2. Window function frequency response. To avoid clutter, the response function is only plotted in detail until $f\tau = 8$, above this a smoothed value is used, as indicated by the dot-dashed line. As well as having good asymptotic behaviour, the Planck-taper window has the narrowest main lobe, except for the rectangular window.

This was put forward for use with binary coalescences, and has superb asymptotic decay. However, the peak sidelobe is high, which is disadvantageous here. We therefore propose a new window function: the Planck-Bessel window which combines the Kaiser-Bessel and Planck-taper windows to produce a window which inherits the best features of both, albeit in a diluted form,

$$w_{\text{PB}}(t; \beta, \epsilon) = w_{\text{P}}(t; \epsilon)w_{\text{KB}}(t; \beta). \quad (\text{A9})$$

The window functions' frequency responses are plotted in Fig. A2. There is no window that performs best everywhere.

Figure A1 shows the computed Fourier transforms for an example EMRB using no window (alternatively a rectangular window), and the Nuttall window.¹⁶ Using the Nuttall window, the spectral leakage is greatly reduced; the peak sidelobe is lower, and the tail decays away as $1/f^3$ instead of $1/f$. The low frequency signal is not appreciably changed.

The choice of window function influences the results as it changes the form of $\tilde{h}(f)$. The variation in results between windows depends upon the signal: variation is greatest for low frequency bursts, as then there is greatest scope for leakage into the detector band; variation is least significant for zoom-whirl orbits as then there are strong signals to relatively high frequencies, and spectral leakage is confined mostly to below the noise level. To quantify the influence of window functions, we studied the diagonal elements of the Fisher matrix from a selection of orbits with periapses ranging from $\sim 10r_g$ – $300r_g$. For orbits with small periapses all five windows (excluding the rectangular window) produced very similar results: the Planck-taper window differed by a maximum of $\sim 0.5\%$ from the others, which all agreed to better than 0.1% . The worst case results came from the lowest frequency orbits, then the Planck-taper window deviated by a maximum of $\sim 30\%$ in the value for the Fisher

matrix elements, the Blackman-Harris deviated by $\sim 20\%$ and the others agreed to better than $\sim 5\%$. The Planck-taper window's performance is limited by its poor sidelobe behaviour; the Blackman-Harris has the worst performance at high frequency.

For this work we have used the Nuttall window. Its performance is comparable to the Kaiser-Bessel and Planck-Bessel windows, but it is computationally less expensive as it does not contain Bessel functions. Results should be accurate to a few percent at worst, and results from closer orbits, which provide better constraints, should be less affected by the choice of window function. Therefore, we are confident that none of our conclusions are sensitive to the particular windowing method implemented.

This paper has been typeset from a TeX/ L^AT_EX file prepared by the author.

¹⁶ The Blackman-Harris, Kaiser-Bessel and Planck-Bessel windows give almost identical results.